Evolution and Formation of Non-metallic Inclusions During Electroslag Remelting of a Heat-Resistant Steel for Ultra-supercritical Power Plants

SHIJUN WANG, CHENGBIN SHI, YUJING LIANG, XIUXIU WAN, and XIN ZHU

This work aims to clarify the evolution and formation mechanisms of non-metallic inclusions during protective argon gas atmosphere electroslag remelting (ESR) of a low-aluminum 9 mass pctCr heat-resistant steel. The pickup degree of both boron and aluminum in liquid steel during protective argon gas atmosphere ESR was lowered with increasing the SiO_2 content of the slag through inhibiting steel–slag reactions. A kinetic model for describing and predicting oxide inclusion removal by slag adsorption was developed. The oxide inclusions from the steel electrode (quaternary MnO-SiO_2-Al_2O_3-CaO) were fully removed through dissociating into their specific chemical species in liquid steel in parallel with absorbing those undissociated inclusions into molten slag before liquid metal droplets enter into the liquid metal pool. The critical sizes of the oxide inclusions through different removal ways in the ESR process were determined. A part of patch-type MnS inclusions was dissociated into soluble sulfur and manganese in liquid steel, whereas the others dissolved into oxide inclusions during the ESR. The inclusions in the liquid metal pool and ingots are the newly born Al_2O_3 (around 80 pct in number fraction) and CaO-Al_2O_3. The formation of oxide inclusions during the cooling and solidification of liquid steel leads to an increase in both the size and number density of inclusions.

I. INTRODUCTION

DEVELOPMENT of ultra-supercritical coal-fired power units is an important strategy to reduce CO_2 emission and improve fuel utilization efficiency. To this end, extensive steel-research-and-development programs around the world have been performing for ultra-supercritical (USC) coal-fired power plants toward higher steam temperature (620 °C to 650 °C-class) and pressure.[1–3] Rotor and main steam pipes are the most critical components of steam turbines and boilers in USC coal-fired power generation units, respectively. In recent years, extensive efforts have been made to develop heat-resistant steel candidates subjected to the steam temperature of 650 °C-class for USC main steam pipes and turbine rotors, such as MARBN, G115, and NPM steel.[2–4]

Electroslag remelting (ESR) is usually used to produce heat-resistant steels for ultra-supercritical turbine rotors and main steam pipes[5–7] mainly because of its superiority in drastically removing non-metallic inclusions and providing optimal solidification structure (reducing segregation and center porosity, etc.) simultaneously. The production of qualified as-cast ingots by ESR is one of the limiting steps in the manufacture of ultra-supercritical turbine rotors and main steam pipes.[8,9] Since ESR is the last stage for refining liquid metal in the whole manufacture chain, targeting the uniformity of chemistry and microstructure of as-cast ingot as well as inclusion control in the ESR process are quite noteworthy.

9pctCr martensitic heat-resistant steels (typically FB2, MARBN, and G115) used for USC main steam pipes and turbine rotors should keep low-aluminum content ($\leq$ 100 ppm) with aim of preventing the decrease in the creep strength and stress fracture toughness.[10,11] It is also required that these martensitic heat-resistant steels contain a few hundred ppm (by mass) of boron for increasing the martensitic microstructure stability and creep strength,[12,13] as well as reducing the coarsening rate of $M_{23}C_6$ carbides along the grain boundaries[2,14]. Aluminum pickup and boron loss of liquid steel often take place as a result of steel–slag reactions during steelmaking of these martensitic heat-resistant steels,

SHIJUN WANG, CHENGBIN SHI, YUJING LIANG, XIUXIU WAN, and XIN ZHU are with the State Key Laboratory of Advanced Metallurgy, University of Science and Technology Beijing (USTB), Beijing 100083, China. Contact e-mail: chengbin.shi@ustb.edu.cn

leading to unqualified chemical compositions.[8,11,15] It is a general strategy that B_2O_3 and SiO_2 are intentionally kept at a certain content level in the slag in order to prevent the loss of boron and silicon as well as aluminum pickup in liquid steel during the ESR.[8,11,15,16] The industrial trials demonstrated that 6 mass pct SiO_2 addition in slag significantly improved the surface quality of as-cast ESR ingot and drawing-ingot operating practice.[17] In addition, the presence of 1 to 10 mass pct of SiO_2 in the slag is unavoidable in many ESR practices (impurity in raw materials and/or slag–metal reaction products during the ESR). The study by Kim et al.[8] showed that the boron contents of the ingots increased with the increase in the B_2O_3 content of slag (from 0 to 2 mass pct) for protective argon gas atmosphere ESR of 9CrMoCoB steel. Fedko et al.[18] found that the boron contents in electroslag remelted ingot are about 4 to 7 times higher than that in the electrode (0.0020 mass pct B) in the case of 0.8 mass pct B_2O_3 addition in 70 mass pct CaF_2-30 - mass pct CaO slag for protective argon gas atmosphere ESR.

Non-metallic inclusions often induce the initiation of stress concentration cracking[19,20] and fatigue cracking[21,22] during hot forging and service process of ultra-supercritical heat-resistant steels, as well as a remarkable decrease in the creep strength.[12,23] The severity of the detriments caused by inclusions is dependent on their number density, size, and chemical compositions. In low-aluminum steel, the oxide inclusions generally are calcium aluminate and/or manganese silicate inclusions. The inclusions with different chemical compositions in consumable electrode basically undergo different evolution trajectories during the ESR, even if these inclusions are of the same types.[24] Unlike Al_2O_3 and $MgO \cdot Al_2O_3$ inclusions, calcium aluminate and/or manganese silicate inclusions usually experience chemistry variation during ESR through slag–metal–inclusion reactions. Shi et al.[16] demonstrated that the reduction of SiO_2 in CaO-Al_2O_3-SiO_2-1 mass pct MgO inclusions was lightened as the increase in the SiO_2 content of the slag during protective argon gas atmosphere ESR (resulting from suppression of soluble aluminum pickup in liquid steel). Wen et al.[25] reported that MnO-SiO_2 inclusions from Q235B steel electrode were modified to Al_2O_3-MnO inclusions in the ingot because of the reaction between soluble aluminum in liquid steel and SiO_2 and MnO in original inclusions during the ESR. Gao et al.[26] found that the soluble Ce (reduced from the slag by soluble aluminum during ESR) in liquid steel reduced MgO in $MgO \cdot Al_2O_3$ inclusions, consequently resulting in the generation of MgO-Al_2O_3-Ce_2O_3 and Al_2O_3-Ce_2O_3 during ESR of FGH96 superalloy.

The evolution of Al_2O_3, $MgO \cdot Al_2O_3$, and some kinds of calcium aluminate and/or manganese silicate inclusions during ESR and its relevance with process parameters of ESR have been assessed in the authors' recent review.[24] The removal degree and evolution of the original inclusions during ESR are largely dependent on the composition and size of these inclusions, as well as more or less on other parameters (slag compositions, liquid metal chemistries, melting rate, and electrical parameters of ESR).[24,27] The detrimental effects of oxide and nitride inclusions to the processing and mechanical properties of heat-resistant steels used for USC turbine rotors and main steam pipes have been well recognized,[12,19–23] there is still a lack of the investigations of the evolution and formation of inclusions during ESR of USC heat-resistant steels (specific to particular steel chemistry).

MARBN and G115 steels have been developed for application to boiler components with maximum steam temperature of 650 °C and as a potential candidate for 650 °C-class USC rotor steel.[3,4,28,29] In the current study, the variation of alloying element content of a heat-resistant steel (based around the general compositions of MARBN and G115 steels) during protective argon gas atmosphere ESR when using the slag with varying SiO_2 contents was ascertained. The evolution of the inclusions from the electrode and generation of fresh inclusions during protective argon gas atmosphere ESR were studied through monitoring the transient inclusions in combination with thermodynamic and kinetic considerations. A kinetic model for describing and predicting oxide inclusion removal during ESR was developed. The influence of different SiO_2 contents in the slag on the oxide inclusions was clarified.

II. EXPERIMENTAL

A. ESR Procedure

The steel electrode was prepared by a vacuum induction melting (VIM) furnace. The liquid steel was cast into a rod of 300 mm in diameter, and thereafter forged into consumable electrode. Table I presents the chemical composition of the consumable steel electrode. The chemical compositions of the pre-melted slag S1, S3, and S5 used for protective argon gas atmosphere ESR trials R1, R3, and R5, respectively, are shown in Table II. Pre-melted slag was roasted at 973 K (700 °C) for 8 hours to remove the moisture.

Steel samples were taken from liquid metal pool during the protective argon gas atmosphere ESR process using a vacuum sampling quartz tube, followed by quenching. Three as-cast ingots produced in the trials R1, R3, and R5 were designated as D1, D3, and D5, respectively.

B. Composition Analysis and Inclusion Characterization

The contents of calcium, silicon and magnesium in the consumable steel electrode and ESR ingots were measured by the inductively coupled plasma atomic emission spectroscopy (ICP-AES). The inductively coupled plasma mass spectrometry (ICP-MS) measurement was performed to analyze the aluminum content of the steel. The inert gas fusion-infrared absorptiometry (EMGA-830, HORIBA, Japan) was employed to measure the total oxygen content of the steel. The sulfur content of the steel was measured by the combustion-infrared absorption technique (EMIA-920V2, HORIBA, Japan).

Table I. Chemical Composition of the Consumable Electrode (Mass Percent)

C	Si	Mn	Cr	Ca	Al	B	O	S	N
0.09	0.46	0.53	8.88	< 0.0005	0.0010	0.0089	0.0054	0.0046	0.0040

Table II. Chemical Compositions of the Slag Used in Protective Argon Gas Atmosphere ESR Trails (Mass Percent)

Slag No.	CaF_2	CaO	MgO	Al_2O_3	SiO_2	B_2O_3
S1	40.85	27.04	0.52	28.97	0.92	1.50
S3	39.13	25.91	0.50	27.75	5.00	1.50
S5	37.46	24.80	0.48	26.57	9.00	1.50

Table III. Chemical Compositions of ESR Ingots (Mass Percent)

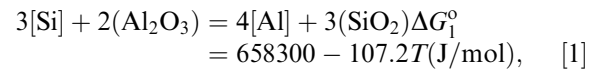| Ingot No.	Si	Al	B	Ca	O	S
D1	0.26	0.0400	0.034	< 0.0002	0.0032	0.0014
D3	0.30	0.0230	0.029	< 0.0002	0.0020	0.0018
D5	0.37	0.0079	0.028	< 0.0002	0.0035	0.0023

Metallographic samples that were taken from the electrode and as-cast remelted ingots, as well as the steel samples that collected from the liquid metal pool were mechanically ground and polished. The cross-sections of these polished steel samples were analyzed by scanning electron microscope (SEM, FEI Quanta-250; FEI Corp., Hillsboro, OR) equipped with energy dispersive X-ray spectrometer (EDS, XFlash 5030; Bruker, Germany) to characterize the inclusions.

An automated SEM instrument (EVO18, ZEISS, Germany) equipped with EDS (X-Max^N, Oxford Instruments, U.K.) and INCA software (Oxford Instruments, U.K.) were used to perform automated inclusion analysis. 17 mm^2 of the polished cross-section was analyzed for each steel sample. The inclusions with an equivalent circle diameter (ECD) smaller than 1 μm were not included in the analysis.
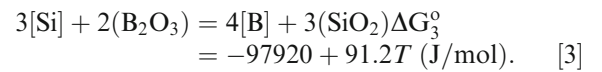
III. RESULTS AND DISCUSSION

A. *Composition Change of the Steel*

The chemical composition of the steel significantly influences the inclusion chemistries. The types and compositions of inclusions may vary depending on the alloy element content of the steel during the ESR. The chemical compositions of the remelted ingots are shown Table III. It can be seen, by comparing the compositions of consumable electrode and remelted ingots, that the aluminum content increases, the silicon content decreases as well as the boron content increases after the protective argon gas atmosphere ESR. The steel–slag reactions, which could lead to the change in the steel compositions, are expressed in Eqs. [1] and [3]. The Gibbs free energy changes for these two steel–slag reactions were calculated.[18,30]

$$3[Si] + 2(Al_2O_3) = 4[Al] + 3(SiO_2)\Delta G_1^o$$
$$= 658300 - 107.2T(J/mol), \quad [1]$$

$$K_1 = \frac{a_{[Al]}^4 \cdot a_{(SiO_2)}^3}{a_{[Si]}^3 \cdot a_{(Al_2O_3)}^2}, \quad [2]$$

$$3[Si] + 2(B_2O_3) = 4[B] + 3(SiO_2)\Delta G_3^o$$
$$= -97920 + 91.2T \ (J/mol). \quad [3]$$

$$K_3 = \frac{a_{[B]}^4 \cdot a_{(SiO_2)}^3}{a_{[Si]}^3 \cdot a_{(B_2O_3)}^2}, \quad [4]$$

where ( ) and [ ] represent the species in the slag and liquid steel, respectively. a_i represents the activity of component i.

Steel–slag reactions would take place at three sites during electroslag remelting: ① electrode tip/slag interface, ② molten metal droplet/slag interface, ③ liquid metal pool/slag interface.[31] The electrode tip/slag interface has been well recognized to be the most dominant site for the chemical reaction because of excellent thermodynamic and kinetic conditions during the formation of liquid metal film, large specific surface area, and adequate reaction time between liquid metal film and slag at the electrode tip.[32–34] It has been reported that the temperature of liquid metal film is close to the liquidus temperature of the steel, and its superheat could hardly exceed 20 K to 30 K (20 °C to 30 °C).[35–37] The solidus and liquidus temperatures of

Table IV. First-Order Interaction Parameters e_i^j Used in the Current Study

$i (j\rightarrow)$	C	Si	Mn	S	Al	Ni	Cr	Ca	Mo	V	O	B
Si	0.18	0.103	− 0.0146	0.066	0.058	0.005	− 0.0003	− 0.066	0.11[42]	0.025	− 0.119	0.2
Al	0.091	0.056	0.035[16]	0.035	0.045[16]	− 0.029[16]	0.0096[16]	− 0.047[16]	—	—	− 1.98[16]	—
B	0.22	0.078	− 0.00086	0.048	—	—	—	—	—	—	− 0.21	0.038
S	0.111	0.075	− 0.026	− 0.046	0.041	—	− 0.0105	− 110	0.0027	− 0.019	− 0.27	—
Mn	− 0.0538	− 0.0327	—	− 0.048	—	− 0.0072	0.0039	—	0.0046	0.0057	− 0.083	—

Note The data without notation are from Ref. [43].

the studied steel calculated with Thermo-Calc (TCFE 8 database) are 1608 K and 1763 K (1335 °C and 1490 °C), respectively. The activities of SiO_2 and Al_2O_3 relative to pure solid standard state, and the activity of B_2O_3 relative to pure liquid standard state in molten slag at 1793 K (1520 °C) were calculated with the reported activity model.[38,39] The activity coefficients of soluble aluminum, silicon and boron in liquid steel were calculated by the following formula:[40]

$$\lg f_i = \Sigma(e_i^j[\text{pct}j] + [r_i^j[\text{pct}j]^2),\qquad[5]$$

where f_i is the activity coefficients of soluble component i in liquid steel. [pct$i$] represents the mass percentage of component i in liquid steel. e_i^j is the first-order interaction parameter. The first-order interaction parameters are shown in Table IV. r_i^j is the second-order interaction parameter, $r_{Al}^C = -0.004$, $r_{Al}^{Si} = -0.0006$, $r_{Si}^{Si} = -0.0055 + 6.5/T$, $r_{Al}^{Al} = -0.0011 + 0.17/T$.[41]

The activity calculation shows that the activities of SiO_2, Al_2O_3, and B_2O_3 increase with the increase in the SiO_2 content of slag. The calculated values of Gibbs free energy change with regard to three protective argon gas atmosphere ESR trials for chemical reaction [1] are − 281.99, − 180.56, and − 120.83 kJ/mol, respectively. The calculated values of Gibbs free energy change for chemical reaction (3) are calculated to be − 248.03, − 171.98, and − 145.76 kJ/mol for R1, R3, and R5 trials, respectively. These thermodynamic calculations indicate that the loss of Si and the pickup of Al and B in the steel are indeed caused by the chemical reactions (1) and (3). It is more SiO_2 addition to the slag in the trial R3 and trial R5 that the pickup of Al and B and the loss of Si in liquid steel are inhibited, as indicated by an increase in the Gibbs free energy change for the chemical reactions [1] and [3]. The present result is consistent with the finding by Kim et al.,[8] who found that the Si recovery was increased with increasing SiO_2 content of the slag, and the Al and B contents were controlled in the target ranges by varying the SiO_2 content of slag. The current study demonstrates that the appropriate amounts of SiO_2 and B_2O_3 addition to the slag would prevent the aluminum pickup and the loss of silicon and boron in heat-resistant steel during protective argon gas atmosphere ESR process.

B. Inclusions in Consumable Steel Electrode

Figure 1 presents an example of inclusions in the consumable steel electrode. All observed oxide inclusions were recognized as quaternary system MnO-SiO_2-Al_2O_3 with approximately 3 mass pct of CaO. Note that these oxide inclusions are accompanied with patch-type MnS inclusions invariably.
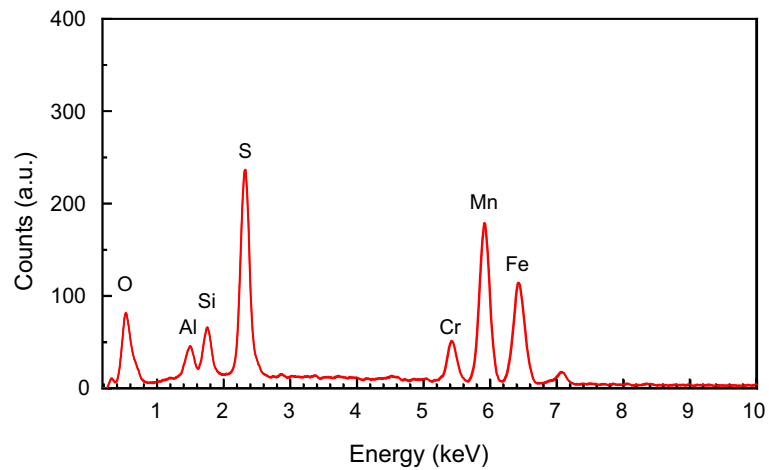
Typical inclusions in the steel electrode are presented in Figure 2. Almost all observed inclusions are larger than 2 μm and associated with more or less patch-type MnS inclusions. The compositions of the oxides in the oxide-sulfide inclusions were plotted on the MnO-SiO_2-Al_2O_3-3 mass pct CaO phase diagram calculated with FactSage 7.2 (FToxid database) (see Figure 3). 100 pct of the oxide inclusion have compositions located
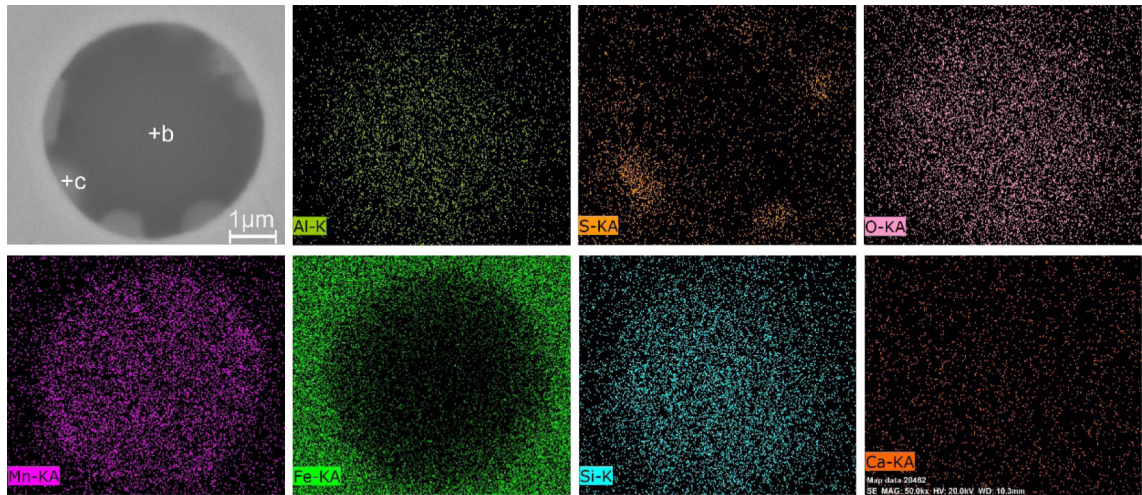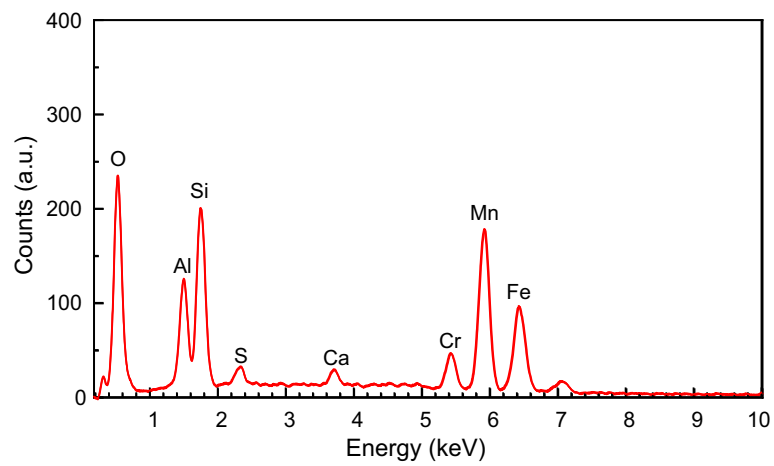
Fig. 1—SEM image and EDS element mappings of a typical inclusion observed in the steel electrode. (*a*) patch-type MnS associated with a MnO-SiO₂-Al₂O₃-CaO inclusion. EDS spectra in (*b*) and (*c*) correspond to the points + b and + c of the inclusion shown in (a), respectively.
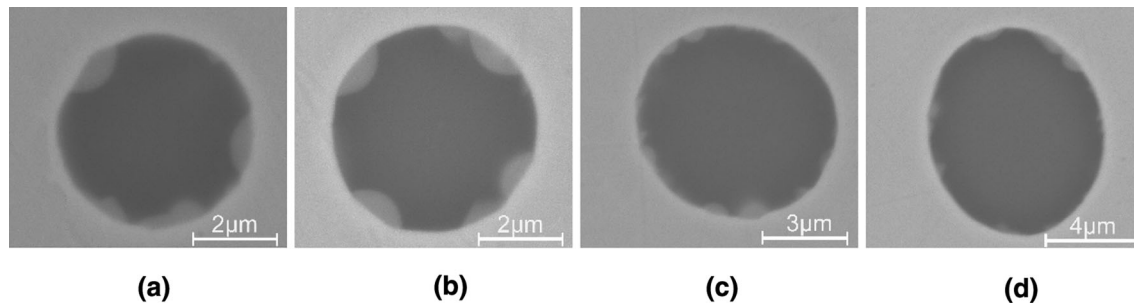
Fig. 2—SEM images of typical inclusions in the steel electrode. (*a*), (*b*), (*c*), and (*d*) MnO-SiO$_2$-Al$_2$O$_3$-CaO attached with more or less patch-type MnS.
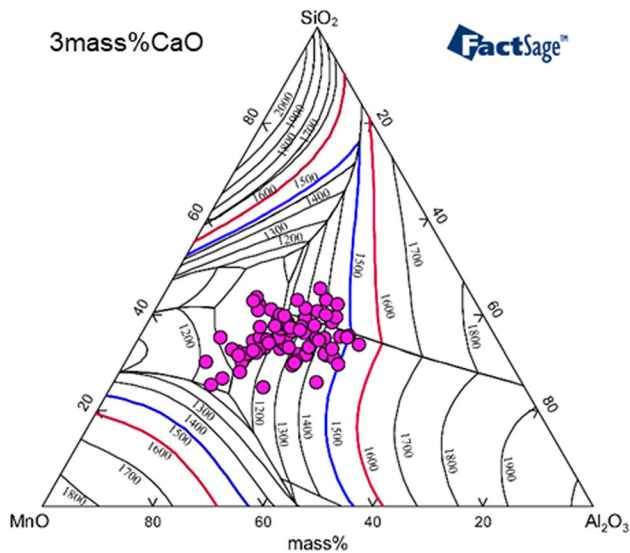

Fig. 3—Oxide inclusions composition at MnO-SiO$_2$-Al$_2$O$_3$-3 mass pct CaO phase diagram (temperature in degrees Celsius). Solid pink circles, some of which overlap each other, represent the composition of the inclusions.

in low-melting-temperature region limited by 1773 K (1500 °C) isotherm, as presented in Figure 3, indicating the liquid state of these oxide inclusions in liquid steel at the steelmaking temperatures.

C. Inclusions in the Liquid Metal Pool and Remelted Ingots

To reveal the evolution of inclusions during the ESR, the inclusions in the steel taken from the liquid metal pool during protective argon gas atmosphere ESR and as-cast ingots were characterized in terms of their compositions and size. Examples of inclusions are shown in Figures 4 through 7. No relics from the consumable electrode without a change are observed in the liquid metal pool. It is noted that the observed inclusions are roughly smaller than that in the electrode. Figure 4 shows the SEM images and EDS spectra of typical inclusions in liquid metal pool in the R1 trials. The inclusions are mainly Al$_2$O$_3$, and the others are binary CaO-Al$_2$O$_3$. The same types of inclusions were

observed in the liquid metal pool of R3 and R5 trials, as shown in Figures 5 and 6. The CaO content of CaO-Al$_2$O$_3$ inclusions in liquid metal pool of trials R1, R3, and R5 increases from 13.65 mass pct, 16.11 mass pct to 20.75 mass pct with increasing SiO$_2$ content of slag from 0.92 mass pct, 5.00 mass pct to 9.00 mass pct. The liquidus temperatures of the CaO-Al$_2$O$_3$ inclusions (based on overall average composition) in the liquid metal pool are predicted with FactSage 7.2 (FToxid database) as 2123 K (1850 °C), 2079 K (1806 °C), and 2037 K (1764 °C) for R1, R3, and R5 trials, respectively, indicating that all CaO-Al$_2$O$_3$ inclusions remain solid state in liquid steel.

The examples of the observed inclusions (EDS element mappings) in ESR ingots are illustrated in Figure 8. Two types of oxide inclusions, *i.e.*, CaO-Al$_2$O$_3$ and Al$_2$O$_3$, were identified in the ingots. The Al$_2$O$_3$ contents of CaO-Al$_2$O$_3$ inclusions are 91.47 mass pct, 90.96 mass pct, and 90.22 mass pct in ingots D1, D3, and D5, respectively. The number proportion of different kinds of oxide inclusions in the electrode, metal pool and ingots are presented in Figure 9. There is no noticeable change in the number proportion of oxide inclusions from liquid metal pool to as-cast ingots (about 80 pct of Al$_2$O$_3$ inclusions in number fraction).

Figure 10 shows the compositions of CaO-Al$_2$O$_3$ inclusions in the liquid metal pool and ingots. The Al$_2$O$_3$ content of CaO-Al$_2$O$_3$ inclusions in ingot is higher than that in liquid metal pool for each protective argon gas atmosphere ESR trial. It should be stressed that no sulfide inclusions were observed in the liquid metal pool for each trial and as-cast ingot.

D. Size and Number Density of Inclusions

The size distribution of the inclusions in the consumable electrode, liquid steel pool and remelted ingot is shown in Figure 11. In this article, equivalent circle diameter of inclusion represents its size unless specially stated. It is noted in Figure 11 that the size of the inclusions decreases and then increases slightly from the consumable electrode to the liquid steel pool then to the electroslag ingot. There are 18.24 pct of inclusions less than 2 μm in size in the consumable electrode, while the number of proportions of inclusions less than 2 μm in size increases significantly after electroslag remelting. The number of proportions of inclusions smaller than
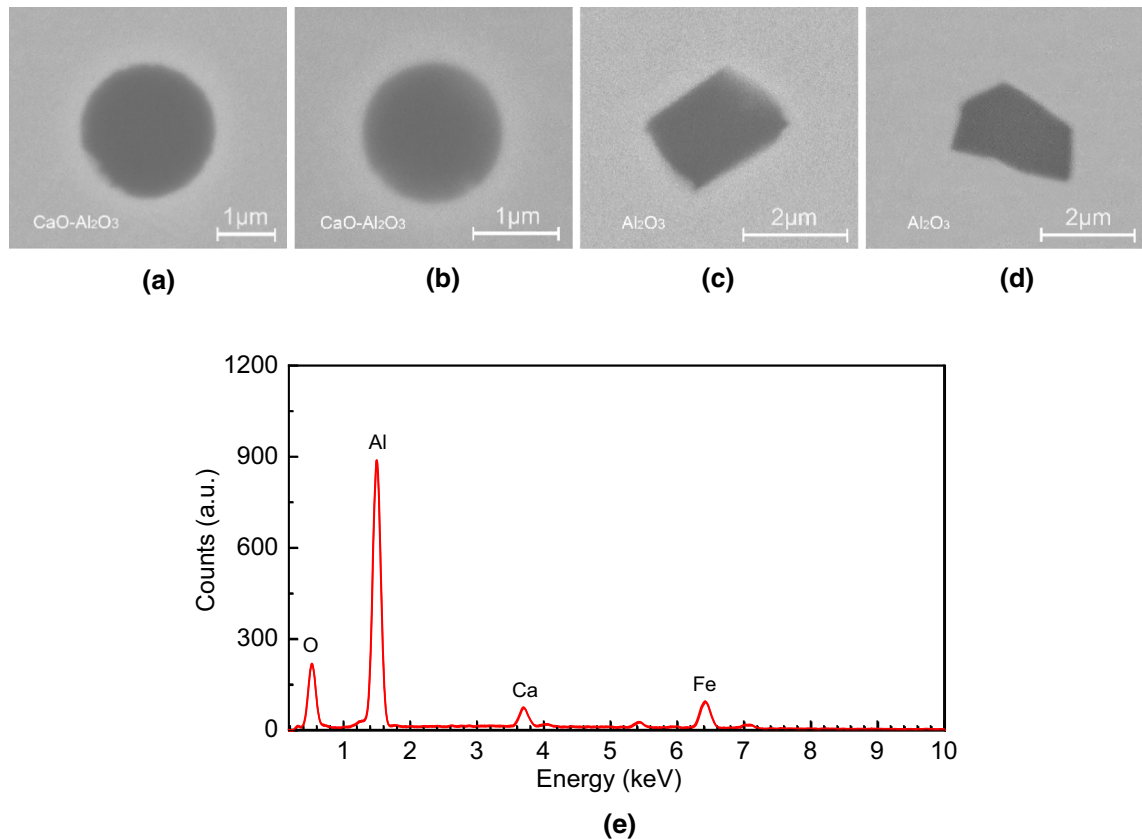
Fig. 4—Examples of inclusions in the steel sampled from the liquid metal pool of R1 trial. (*a*) and (*b*) CaO-Al$_2$O$_3$, (*c*) and (*d*) Al$_2$O$_3$. (EDS spectrum shown in (*e*) corresponds to the oxide inclusion shown in (*a*)).

2 μm in the R3 liquid steel pool is the largest, at 47.06 pct. Moreover, the number of proportions of inclusions larger than 5 μm was significantly reduced after electroslag remelting, in which the number proportion of the inclusions larger than 5 μm in D3 ingot was the smallest (7.69 pct). The number proportion of the inclusions larger than 4 μm in D1 and D5 ingots are higher than that of the inclusions larger than 4 μm in the liquid steel pool, and the ratio of inclusions smaller than 2 μm in D3 is lower than that of inclusions smaller than 2 μm in the liquid steel pool. It was reported that the oxygen content level of the steel could affect the size of oxide inclusions.[44] As shown in Figure 11, the oxygen content of the steel decreases after electroslag remelting, resulting in a reduction in the size of the inclusions accordingly.

The relationship between number density and size of inclusions during the protective argon gas atmosphere ESR process is shown in Figure 12. As shown in Figure 12, the number density of all inclusions with different sizes decreases significantly after protective argon gas atmosphere ESR. It can be learned that the number density of the inclusions with different size in each as-cast ingots is larger than that in the steel sampled from the liquid steel pool. The inclusions in the liquid steel pool and ESR ingot are mainly in the size

range of 1 to 3 μm. The current experimental results show that the inclusions in the consumable electrode have been fully removed before entering the liquid metal pool, and the inclusions in the liquid metal pool are newly formed. During the cooling and solidification of liquid steel at the bottom of the liquid steel pool, more fresh oxide inclusions are generated (as discussed in Section III–F), accompanying with growth of inclusions, consequently causing an increase in the number and size of inclusions in the remelted ingots.

E. *Mechanism of Oxide Inclusion Removal During Protective Argon Gas Atmosphere ESR*

The equilibrium module of FactSage 7.2 (FToxid and FSstel databases) was used to calculate the formation and transformation of inclusions as well as the variation of inclusion-forming elements contents in steel with the temperature. The transformation of the inclusions in the consumable electrode with temperature is shown in Figure 13(a). It can be seen from Figure 13(a) that non-metallic inclusions are gradually precipitated as the temperature decreases. The liquid inclusions start to form when the temperature is decreased to 1942 K (1669 °C), and show an increasing trend in amount until 1623 K (1350 °C). The thermodynamic calculation
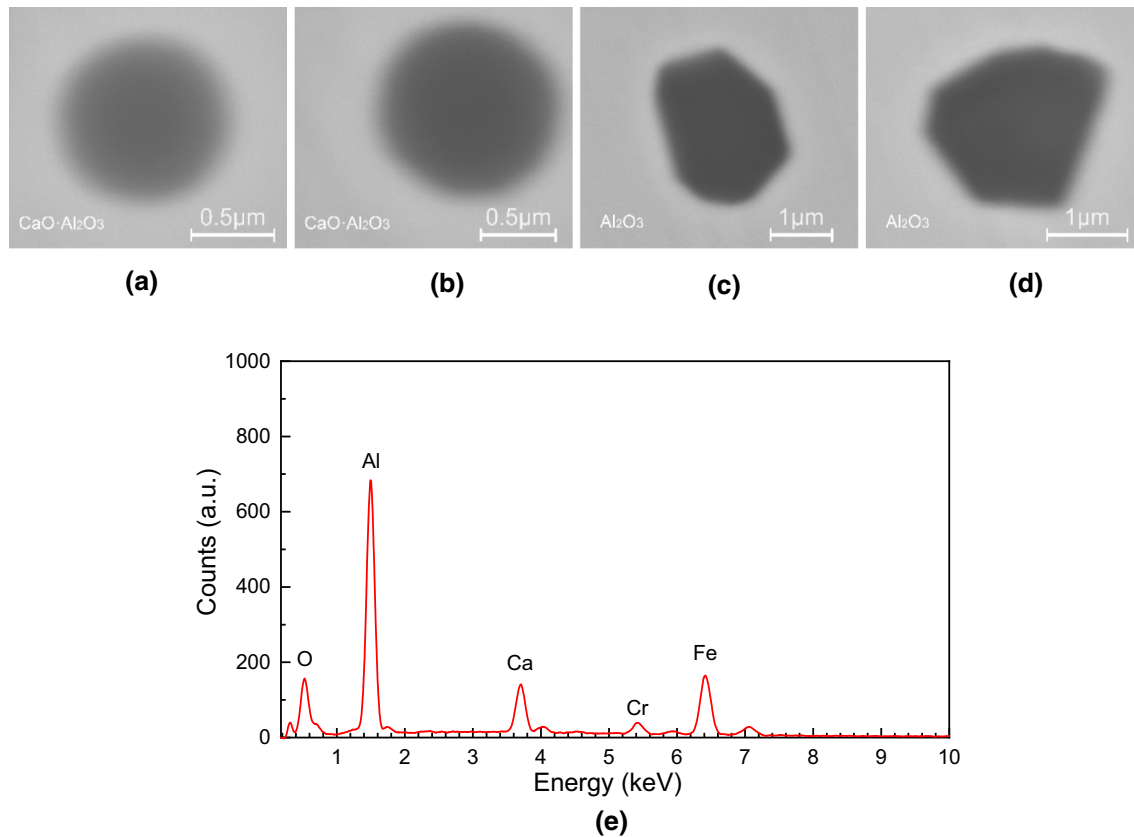
Fig. 5—Typical inclusions in the steel sampled from the liquid metal pool of R3 trial. (*a*) and (*b*) CaO-Al₂O₃, (*c*) and (*d*) Al₂O₃. (EDS spectrum shown in (*e*) corresponds to the oxide inclusion shown in (a)).

shows that the liquid inclusion consists of the MnO, SiO₂, Al₂O₃, and CaO as shown in Figure 13(b), which is consistent with the experimentally observed inclusions in the electrode. According to the thermodynamic equilibrium calculation, MnS, SiO₂, Mn₂Al₄Si₅O₁₈, and CaAl₂Si₂O₈ inclusions would precipitate gradually when the temperature is lower than 1623 K (1350 °C). As described in Section III–B, all detectable oxide inclusions in the consumable electrode are liquid MnO-SiO₂-Al₂O₃-CaO. The absence of other types of oxide inclusions is expected to be due to insufficient diffusion of the elements in the solid steel (the thermodynamic calculation with FactSage shows that these inclusions are precipitated in the solid steel at equilibrium state).

Figure 13(a) shows that the amount of liquid inclusions decreases during the heating up and melting of the consumable electrode, in parallel with an increase in soluble oxygen, manganese, silicon, aluminum and calcium in steel (see Figures 13(c) and (d)), reflecting dissociation of liquid inclusions into their individual chemical species into the liquid steel. It can also be learned in Figure 13(a), there are still some liquid inclusions remaining in the steel at the temperature of 30 K (30 °C) above the liquidus temperature of steel. However, there are no inclusions (which are the relics (original inclusions) from the electrode) in liquid steel pool and remelted ingots. It indicates that the inclusions in electrode would be removed fully before entering the

liquid steel pool. The finding in the current study is consistent with the experimental observations reported by Evseyev *et al.*,[45] Shi *et al.*,[46] and Dong *et al.*[47] Apart from the removal by decomposing into liquid steel, the absorption by molten slag is also a way of inclusion removal during the ESR. As pointed out by Baligidad,[48] the liquid metal films at the electrode tip contributed to the removal of inclusions by slag adsorption.

The removal of an oxide inclusion by molten slag at slag–steel interface in the ESR process is schematically illustrated in Figure 14. This removal process consists of four stages, *i.e.*, Stag I: Inclusion just reaches the steel–slag interface. Stag II: Inclusion is crossing the steel–slag interface. Stag III: Inclusion is about to leave the steel–slag interface completely. Stag IV: Inclusion is dissolving in the slag bulk. The free energy change for the inclusion absorption by molten slag ΔG_s at the electrode tip can be expressed as Eq. [6].[49]

$$\Delta G_s = 4\pi r^2 \sigma_{i-s} + \Delta \overline{G} - 4\pi r^2 \sigma_{m-i} - n4\pi(r+\delta)^2 \sigma_{m-s},$$
[6]

where r is the radius of inclusion. σ_{a-b} is the interfacial tension of phase a and b. $\Delta \overline{G}$ is the free energy change for the dissolution of the inclusion in slag. n is the ratio of the surface area of the part that gets into the slag phase of an inclusion to the total surface area of the inclusion (only for the case where there is a liquid
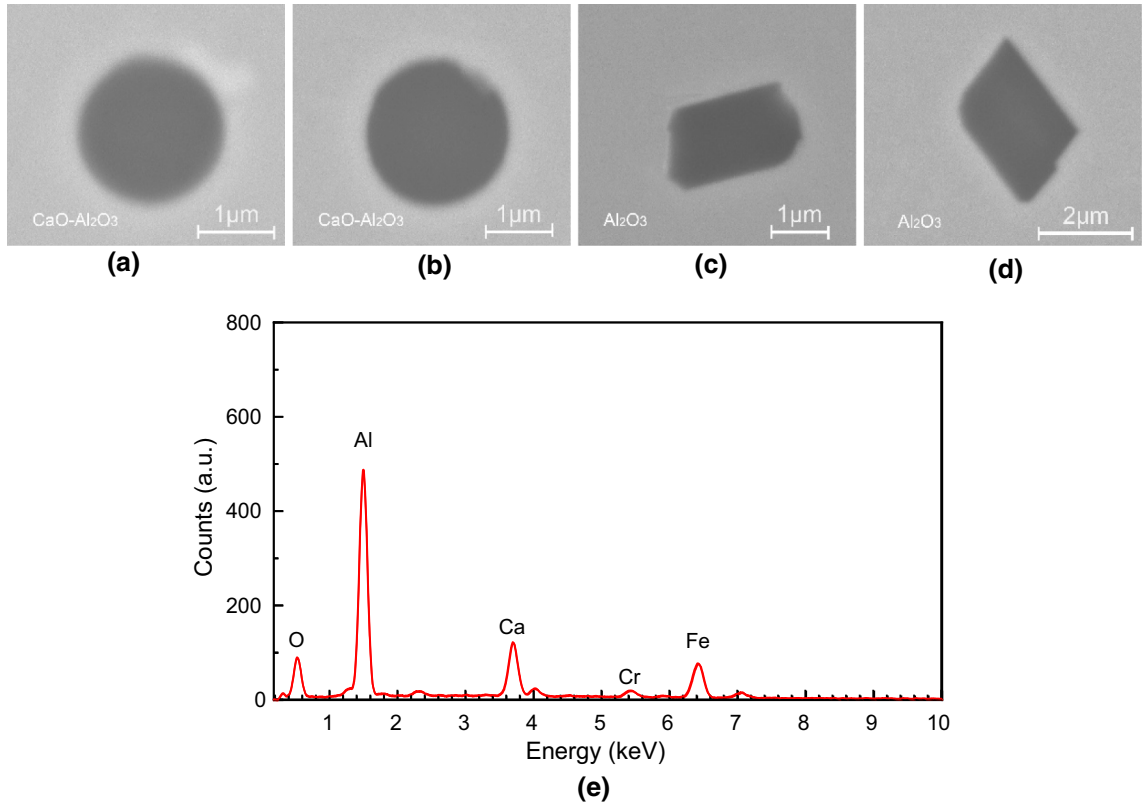
Fig. 6—Examples the liquid metal pool of R5 trial. (*a*) and (*b*) CaO-Al$_2$O$_3$, (*c*) and (*d*) Al$_2$O$_3$. (EDS spectrum shown in (*e*) corresponds to the oxide inclusion shown in (a)).

steel film around the inclusion). δ is the thickness of liquid steel film around inclusion. It is considered that there is no film covering outside of liquid inclusion because of the small size of the inclusion, the values of both n and δ therefore are taken as 0.

In the case of $\Delta G_s < 0$, the inclusions would be removed spontaneously by slag adsorption. The free energy change for the inclusion dissolution in the slag can be neglected by considering the effect of interfacial energy between steel and slag, steel and inclusion, and inclusion and slag. For the case of $\Delta G_s < 0$, the following equation is obtained.

$$4\pi r^2(\sigma_{i-s} - \sigma_{m-i}) < 0. \qquad [7]$$

It can be obtained from Eq. [7] that the decrease in the interface energy between inclusion and slag σ_{i-s}, the increase in the interface energy between liquid steel and inclusion σ_{m-i} is more favorable to remove the inclusions by slag adsorption.

The interfacial tension between phase a and phase b can be expressed as Eq. [8].[50, 51]

$$\sigma_{a-b} = \sigma_a + \sigma_b - 2\phi(\sigma_a\sigma_b)^{0.5}, \qquad [8]$$

where σ_i is surface tension for phase i, ϕ is the interfacial parameter of phase a and phase b, and can be expressed as $\phi = 0.5 + 0.3X_{FeO}$ for the interface of steel–slag and the interface of inclusion–steel.[52] ϕ is taken as 0.5 for the interface between inclusion and slag.[52]

The surface tension of liquid steel can be expressed as Eq. [9][53]:

$$\sigma_M = 1910 - 825 \times lg(1 + 210 \times [\text{mass pct O}]) - 540 \\ \times lg(1 + 185 \times [\text{mass pct O}]).$$

$$[9]$$

The calculated value of σ_M is 1.494 N/m by Eq. [9]. The surface tension of molten slag and inclusion can be obtained from Eq. [10][50]:

$$\sigma_S = X_1\sigma_1 + X_2\sigma_2 + X_3\sigma_3 + X_4\sigma_4 + \cdots + X_n\sigma_n. \qquad [10]$$

Based on the reported value of the surface tension of each component in the slag and oxide inclusions[53,54], the values of surface tension of molten slag (slag S3) and MnO-SiO$_2$-Al$_2$O$_3$-CaO inclusions (according to their average composition in the consumable electrode) were calculated to be 0.464 and 0.493 N/m, respectively. The values of the interfacial tension of steel–slag, inclusion–steel, and slag–inclusion can be calculated as 1.051 N/m, 1.130 N/m, and 0.479 N/m, respectively. Thus, Eq. [7] is proved to be valid. It indicates that the inclusions would be spontaneously absorbed by molten slag thermodynamically at the electrode tip during the ESR process.

For a better understanding of the inclusion removal during the ESR, a mathematical model was developed to describe the behavior of inclusions at the steel–slag interface at the electrode tip and to predict the removal of oxide inclusions during electroslag remelting. The
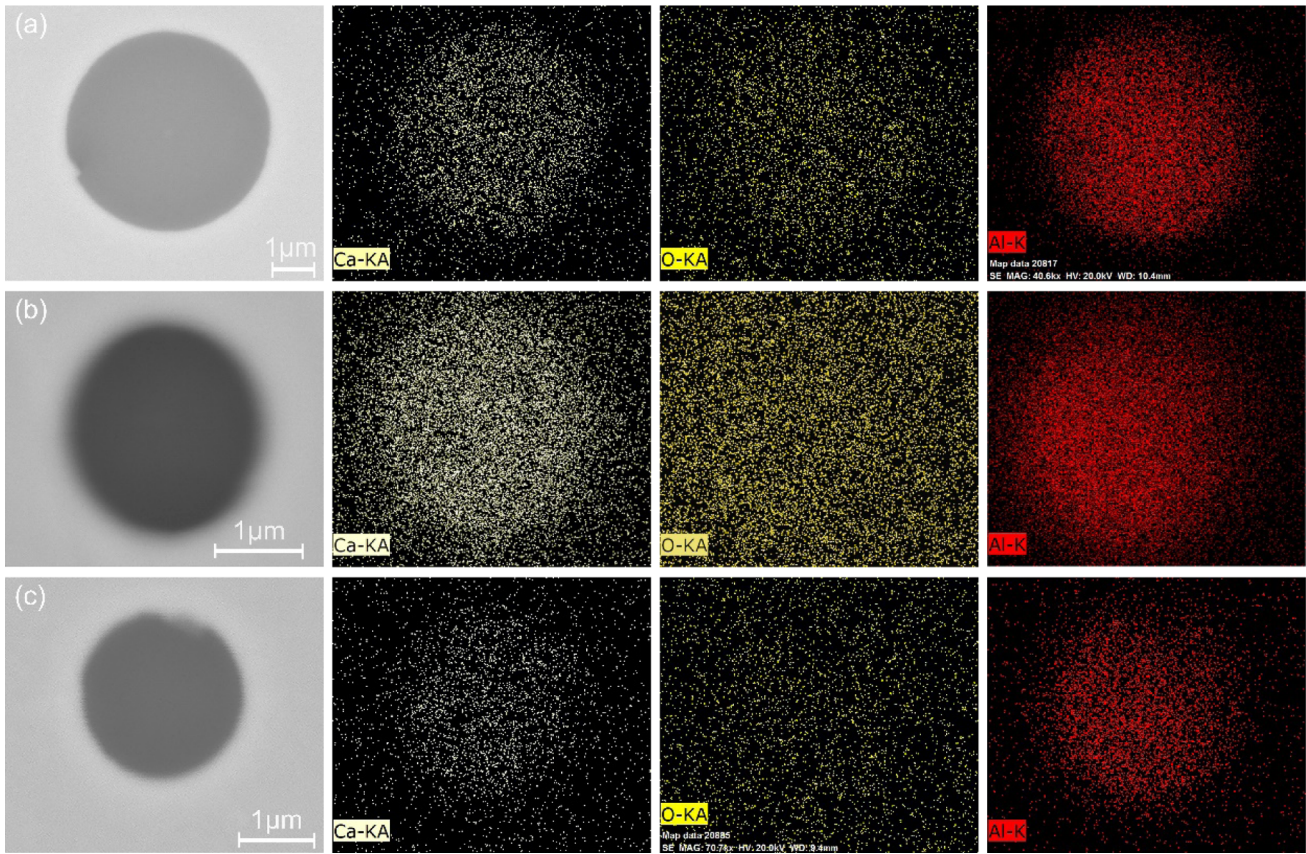
Fig. 7—Element mappings of CaO-Al$_2$O$_3$ inclusions in the liquid metal pool. (*a*) R1 trial, (*b*) R3 trial, and (*c*) R5 trial.

velocity of inclusions, which stay away from steel–slag interface, are assumed to be zero. It is considered that no liquid steel film around inclusion because the inclusion is too small (the inclusion Reynolds number is smaller than unity[55]). For simplifying the calculation, the following assumptions are introduced.

(1) Axially symmetric flow.
(2) Inclusions are considered as spherical since they are small in size.
(3) Creeping flow.
(4) Isothermal incompressible fluid.
(5) Interfacial tension of slag–steel, steel–inclusion, and slag–inclusion is constant.
(6) The original position of the inclusions is just above the slag at the steel–slag interface. The inclusions would be completely separated into slag phase when the displacement exceeds inclusion diameter.

Force diagram of inclusion is schematically illustrated in Figure 14. Seven different forces are considered to contribute to the transfer of inclusions, which include gravity force F_g, buoyancy force F_b, drag force F_d, added mass force F_a, lift force F_l, electromagnetic pressure force F_p, and rebound force F_r.[56]

The gravity force, acting downward, is given by Eq. [11].

$$F_g = mg = \frac{4}{3}\rho_i g \pi r_i^3, \qquad [11]$$

where ρ_i is the density of inclusion. g is gravitational acceleration, and takes as 9.8 m/s^2. r_i is the radius of inclusion.

The buoyancy force is upward, and is described by Eq. [12].

$$F_b = \frac{4}{3}\pi r_i^3 g(A(Z^*)\rho_s - \rho_i), \qquad [12]$$

where Z^* is the dimensionless displacement of the inclusion from its initial position, $Z^* = Z/r_i$, Z is the displacement of inclusion. $A(Z^*) = \frac{1}{4}\left(\frac{\rho_m}{\rho_s} - 1\right)Z^{*3} - \frac{3}{4}\left(\frac{\rho_m}{\rho_s} - 1\right)Z^{*2} + \frac{\rho_m}{\rho_s}$, ρ_m, ρ_s and ρ_i are the density of steel, slag and inclusion, respectively. The values of ρ_m, ρ_s and ρ_i are taken as7.0 g/cm^3, 2.6 g/cm^3 and 3.0 g/cm^3.[57]

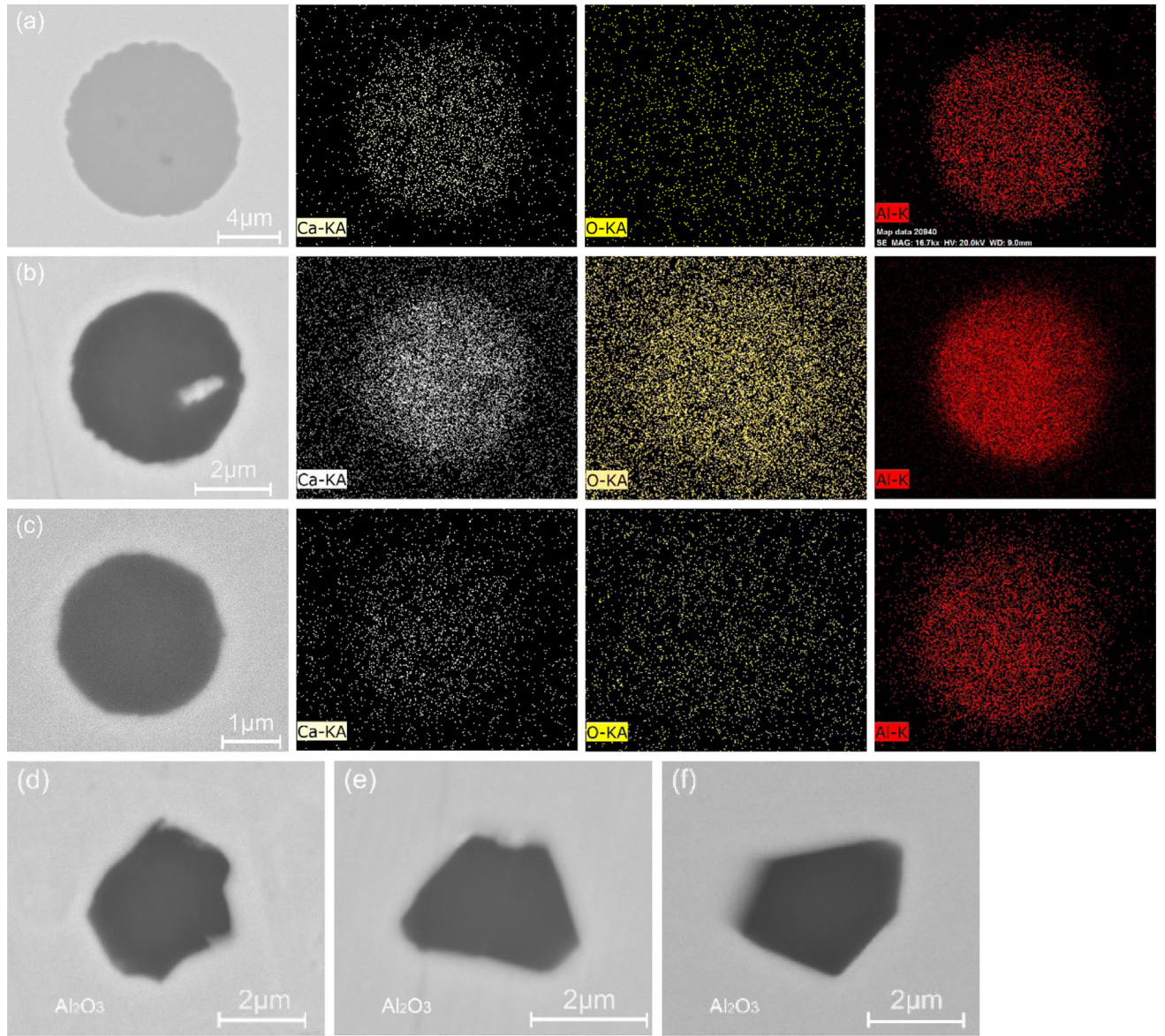The drag force, positive in the upward direction, is given by Eq. [13].

Fig. 8—BSE images and EDS element mappings of typical inclusions observed in the remelted ingots. (a) CaO-Al$_2$O$_3$ in D1, (b) CaO-Al$_2$O$_3$ in D3, (c) CaO-Al$_2$O$_3$ in D5, (d) Al$_2$O$_3$ in D1, (e) Al$_2$O$_3$ in D3, (f) Al$_2$O$_3$ in D5.

$$F_d = 4\pi\sqrt{r_i^3 g} \cdot \mu_s \cdot B \cdot C(Z^*)\frac{dZ^*}{dt^*}, \qquad [13]$$

where t^* is the dimensionless time, $t^* = t\sqrt{g/r_i}$. t is the time for inclusions movement.. $B = \frac{2+3\frac{\mu_i}{\mu_m}}{2\left(1+\frac{\mu_i}{\mu_m}\right)} C(Z^*) = \left(\frac{\mu_m}{\mu_s} - 1\right)Z^{*2} - 2\left(\frac{\mu_m}{\mu_s} - 1\right)Z^* + \frac{\mu_m}{\mu_s}$, μ_m, μ_s and μ_i are the viscosity of liquid steel, slag and inclusion, respectively. The viscosity of liquid steel is taken as 0.006 Pa·s.[55] The viscosities of slag and oxide inclusion are calculated by FactSage 7.2 (viscosity module) to be 0.04 Pa·s and 0.421 Pa·s, respectively.

The added mass force, positive in the downward direction, is described by Eq. [14].

$$F_a = \frac{2}{3}\pi r_i^3 g\rho_s A(Z^*)\frac{d^2 Z^*}{dt^{*2}}, \qquad [14]$$

Lift force is from rotation of the inclusion caused by the velocity gradient of the melt, electromagnetic pressure force is in the horizontal direction, given by Eqs. [15] and [16].[58,59]

$$F_l = -6.46\mu r_i^2(v_i - v)\mathrm{sgn}(G)\left(\frac{\rho|G|}{\mu}\right), G = \frac{dv}{dn}, \qquad [15]$$

$$F_p = -\frac{2(\delta - \delta_i)}{2\delta + \delta_i}\pi r_i^3 F_e, \qquad [16]$$

where μ is the viscosity of mixture phase. v_i and v are the velocity of inclusion and melt, respectively. δ_i and δ are the electrical conductivity of inclusion and mixture phase, respectively. F_e is Lorentz force.
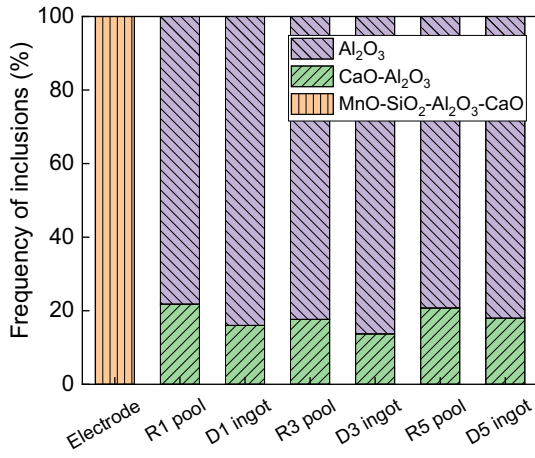
Fig. 9—Relative proportion (number) of oxide inclusions in the electrode, liquid metal pool and remelted ingots.
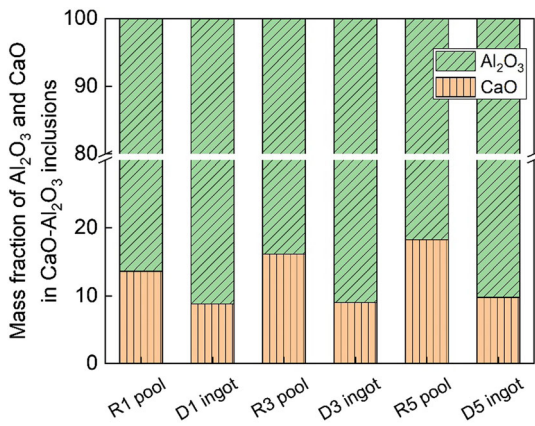

Fig. 10—Composition of CaO-Al$_2$O$_3$ inclusions in the liquid metal pool and remelted ingots.
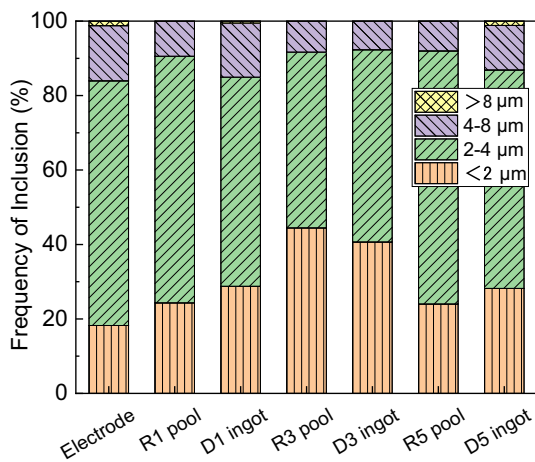

Fig. 11—Size distribution of the inclusions in the electrode, liquid metal pool and ingots.
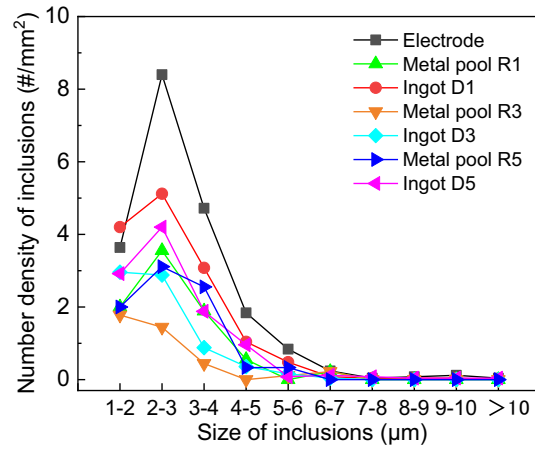

Fig. 12—Relationship between number density and size of inclusions in the electrode, liquid metal pool and remelted ingots.

The rebound force, positive in the upward direction, can be expressed as Eq. [17].

$$F_r = \frac{dE_r}{dZ} = 2\pi r_i \sigma_{m-s} D(Z^*),$$ [17]

where E_r is the change of interfacial energy caused by inclusions transferring across the steel–slag interface, $E_r = -\pi(2r_i Z - Z^2)\sigma_{m-s} + 2\pi r_i Z \sigma_{i-s} + 2\pi r_i(2r_i - Z)\sigma_{i-m}$. $D(Z^*) = Z^* - 1 - \cos\theta_{ims}$, θ_{ims} is the contact angle of inclusion and slag. $\cos\theta_{ims} = \frac{\sigma_{i-m} - \sigma_{i-s}}{\sigma_{m-s}}$. When $\cos\theta_{ims} > 0$, molten slag spreads over the surface of the inclusion, suggesting that the inclusion would enter molten slag bulk.

In the vertical direction, the equation of inclusion motion can be written as:

$$F_g + F_a - F_b - F_d - F_r = ma = \frac{4}{3}\pi r_i^3 \rho_i g \frac{d^2 Z^*}{dt^{*2}}.$$ [18]

Eq. [18] can be rewritten as follows:

$$\frac{d^2 Z^*}{dt^{*2}} = g - \frac{2(\rho_s A(Z^*) - \rho_i)}{(\rho_s A(Z^*) + 2\rho_i)} - \frac{3\sigma_{m-s}}{r_i^2 g(\rho_s A(Z^*) + 2\rho_i)} D(Z^*)$$
$$- \frac{6B\mu_s}{\sqrt{r_i^3 g(\rho_s A(Z^*) + 2\rho_i)}} C(Z^*) \frac{dZ^*}{dt^*}.$$

[19]

The numerical solution was obtained by Python program using the fourth-order Runge–Kutta–Gill method. The behavior of inclusions with radius of 1.0, 1.5, 1.9, 1.95, 2.0, and 3.0 μm was calculated at the steel–slag interface of the electrode tip, results are shown in Figure 15. When the displacement of the inclusions is greater than the diameter of the inclusions, the
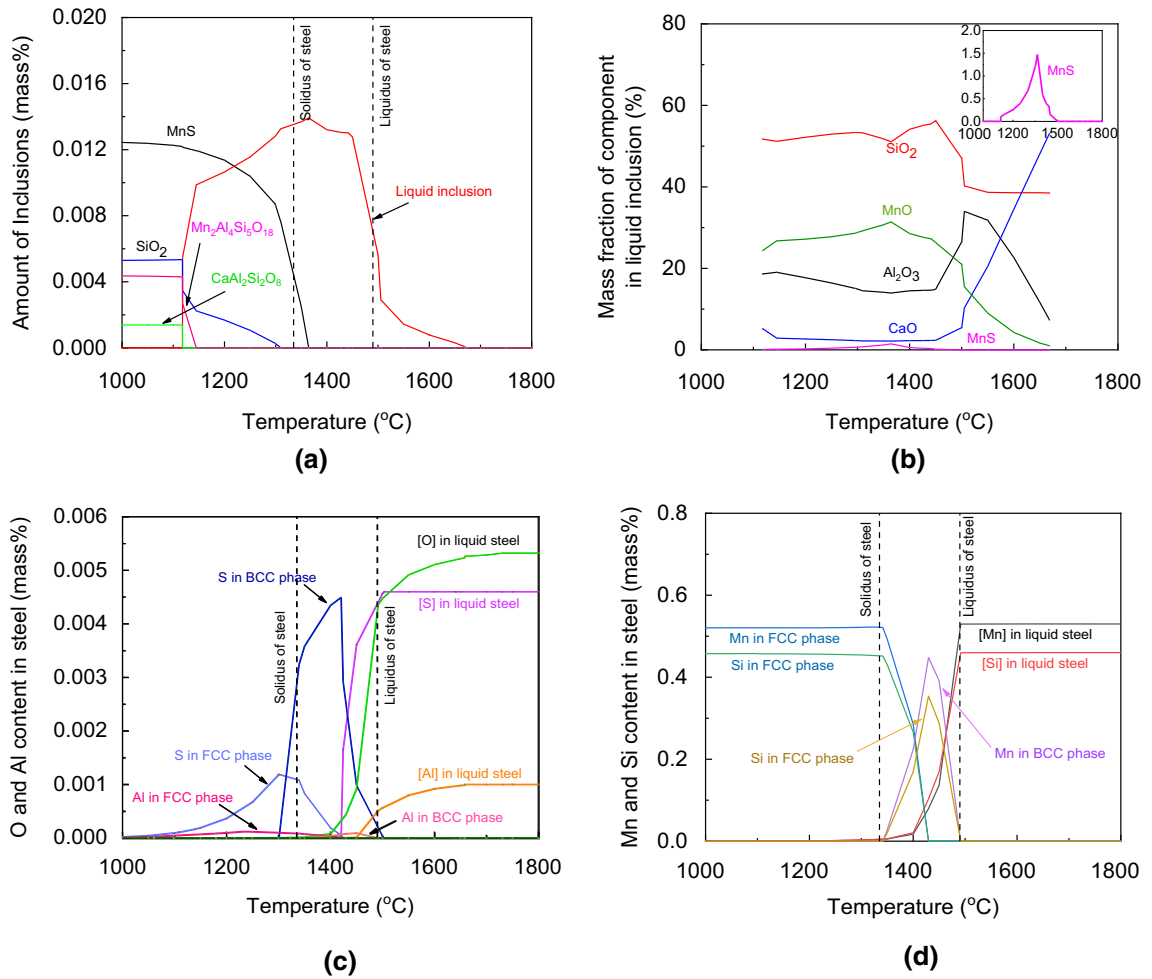
Fig. 13—(*a*) Transformation of inclusions with the temperature in the steel electrode at an equilibrium state, (*b*) the change in the concentrations of the components of liquid inclusion with temperature, (*c*) the variation of the contents of sulfur, aluminum and oxygen in steel with temperature, and (*d*) the variation of the contents of silicon and manganese in steel with temperature calculated with FactSage 7.2.
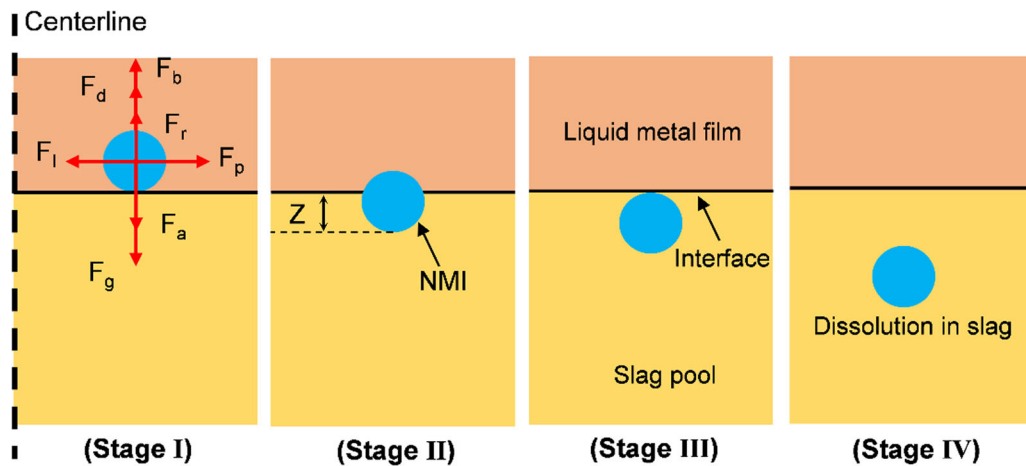

Fig. 14—Force diagram of inclusion and schematic illustration of the removal process of inclusion by slag absorption at the steel–slag interface in electroslag remelting. (NMI represents non-metallic inclusion).

inclusions are said to cross the steel–slag interface and enter into the slag. Dimensionless displacement Z^* is defined as the ratio of displacement and radius of inclusion, The inclusions are therefore considered to be fully absorbed by molten slag when $Z^* \geq 2$.

It can be seen from Figure 15 that the final dimensionless displacement of the inclusions is smaller than 2 when the radius of inclusion is 1.0 or 1.5 μm. When the radius of inclusion is 1.9 μm, the maximum value of dimensionless displacement of the inclusion reaches 1.98 but is still smaller than 2, indicating that the inclusion with a radius no more than 1.9 μm cannot be allowed to enter the slag. When the radius of the inclusion is 1.95 μm, Z^* has just increased to 2.00. In this case, the inclusions can cross the steel–slag interface and move into the molten slag bulk. Inclusions with the radius of 2 μm can enter into slag because the dimensionless displacement is 2.02. The dimensionless displacement of the inclusions is 2.35 when the inclusion with a radius of 3.0 μm and can enter into the slag. Inclusion with a larger radius is in favor to have a larger dimensionless displacement. It indicates that the critical diameter of the inclusion that can cross the steel–slag interface and move into slag is 3.9 μm. Therefore, the inclusions larger than 3.9 μm can cross the slag–steel interface and absorbed by slag during the ESR. According to the statistical results shown in Figure 11, 16 pct of oxide inclusions (in number fraction) from the electrode would be removed through being absorbed by molten slag at electrode tip. The residence time of the liquid metal film at the electrode tip is about 1 to 3 seconds during ESR.[37,60,61] The current study shows that the time for inclusion absorption by molten slag is less than 10^{-5} s. Therefore, sufficient residence time is available for inclusion to cross the steel–slag interface and be removed by slag adsorption.

During the current protective argon gas atmosphere ESR process, the oxide inclusions in the consumable electrode have been removed in two ways: (I) in the process of electrode heat-up, the liquid oxide inclusions dissociated as dissolved manganese, silicon, aluminum, calcium and oxygen in the molten steel, which entered the molten droplets at the electrode tip and passed through the slag pool with the molten droplets and then moved into the molten pool. (II) the inclusions larger than 4 μm in size passed through the steel–slag interface and were removed by slag adsorption.

The inclusion observations in the current study show that all MnS inclusions from the electrode are removed before liquid metal droplets enter into the liquid metal pool (see Section III–C). The formation of patch-type MnS inclusion around oxide inclusion has been clarified in previous studies.[62] The trajectory of patch-type MnS inclusions removal may be different from that of single-phase MnS and oxide inclusions. The question whether the removal of patch-type MnS inclusions holds different mechanisms still remains during ESR. A thermodynamic calculation was made to assess the patch-type MnS inclusion removal through the interaction between liquid steel and MnS inclusions[63].
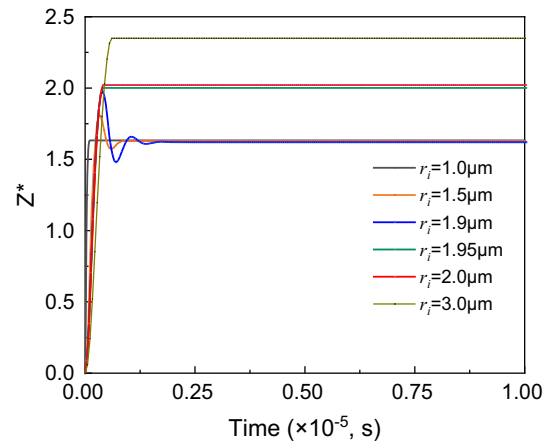

Fig. 15—Displacement of the inclusions at the steel–slag interface of electrode tip with different sizes at time t for the case with no steel film.

$$(MnS)_{inclusion} = [Mn] + [S]\Delta G_{20}^o$$
$$= 168822 - 98.87T(J/mol), \quad [20]$$

$$K = \frac{a_{[Mn]} \cdot a_{[S]}}{a_{(MnS)}} = \frac{f_{[Mn]}[pctMn]f_{[S]}[pctS]}{a_{(MnS)}}, \quad [21]$$

where $a_{(MnS)}$ is the activity of MnS. The activity coefficients of soluble aluminum and silicon in liquid steel $f_{[Mn]}$ and $f_{[S]}$ can be calculated with formula [5] in combination with the first-order interaction parameters summarized in Table IV and available second-order interaction parameters as:[30] $r_S^C = 0.0058$, $r_S^{Si} = 0.0017$, $r_S^S = -0.0009$, $r_S^{Al} = 0.0009$.

The temperature of the liquid metal film was taken as the liquidus temperature of the steel because its superheat could hardly exceed 20 K to 30 K (20 °C to 30 °C).[35–37] The Gibbs free energy change for reaction [20] is evaluated to be -95.42 kJ/mol at 1763 K (1490 °C). This very negative Gibbs free energy change would confirm the dissociation of MnS inclusions into soluble sulfur and manganese in liquid steel during the formation of liquid metal films and subsequent their collection into metal droplets. This is supported by thermodynamic calculation with FactSage showing that the amount of MnS inclusions decreases, in parallel with an increase of the soluble sulfur content in steel, as increasing the temperature of the electrode (see Figures 13(a) and (c)).

It can be learned from Figure 13(b) that the concentration of MnS in liquid MnO-SiO$_2$-Al$_2$O$_3$-CaO inclusion increases with increasing the temperature up to 1364 °C, indicating the dissolution of MnS into liquid oxide inclusion. KTH model, as expressed in Eq. [22][64], has been widely used to predict the sulfide capacity of oxide melts. In the current study, KTH model was employed to calculate the sulfide capacity of MnO-SiO$_2$-Al$_2$O$_3$-CaO inclusions.

$$C_s = \exp\left(-\frac{\Delta G^o}{RT}\right) \cdot \exp\left(-\frac{\xi}{RT}\right), \qquad [22]$$

where C_s is sulfide capacity. ΔG^o is the standard Gibbs free energy change for reaction [23].

ξ in a multicomponent system is described as a function of both temperature and composition, as expressed in Eq. [24].

$$\frac{1}{2}\{S_2\} + (O^{2-}) = \frac{1}{2}\{O_2\} + (S^{2-}) \Delta G^o_{23}$$
$$= 118535 - 58.8157T^{[64]} \,(J/mol), \qquad [23]$$

where { } represents the species in the gas.

$$\xi = \sum (X_i \xi_i + \xi_{mix}), \qquad [24]$$

where X_i represents mole fraction of component i in oxide melts. ξ_i is expressed as a linear function of the temperature for each component in the oxide melts in the absence of interaction between different species. ξ_{mix} represents the mutual interaction (binary and ternary) between different species. The expression of ξ for MnO–SiO$_2$–Al$_2$O$_3$–CaO melts is presented as follows:

$$\xi = X_{MnO}\xi_{MnO} + X_{SiO_2}\xi_{SiO_2} + X_{Al_2O_3}\xi_{Al_2O_3}$$
$$+ X_{CaO}\xi_{CaO} + \xi_{mix}^{Al_2O_3-CaO}$$
$$+ \xi_{mix}^{Al_2O_3-MnO} + \xi_{mix}^{Al_2O_3-SiO_2} + \xi_{mix}^{CaO-SiO_2} \qquad [25]$$
$$+ \xi_{mix}^{MnO-SiO_2} + \xi_{mix}^{Al_2O_3-CaO-SiO_2}$$
$$+ \xi_{mix}^{Al_2O_3-MnO-SiO_2} + \xi_{mix}^{CaO-MnO-SiO_2}.$$

The parameters included in Eq. [25] are summarized in Table V. In Table V, y_i represents the cation fraction of cation i, defined as the number of the cations of i N_i over the total number of the cations $\sum_{j=1}^{n} N_j$:[64]

$$y_i = \frac{N_i}{\sum_{j=1}^{n} N_j}. \qquad [26]$$

The sulfide capacity of MnO-SiO$_2$-Al$_2$O$_3$-CaO inclusion (based on overall average composition) at different temperatures predicted by KTH model is presented in Figure 16. The sulfide capacity increases with the increase in the temperature, suggesting dissolution of patch-type MnS into MnO-SiO$_2$-Al$_2$O$_3$-CaO inclusions during heating up and the melting of steel electrode in the ESR process. With continuous increase in the temperature, patch-type MnS along with these oxide inclusions would dissociate as their individual chemical species into liquid steel (see Figures 13(a) and (b)), whereas all undissociated MnS and oxide inclusions from the electrode are removed by absorbing them into molten slag before liquid metal droplets enter into the liquid metal pool (no inclusion relics from the electrode were observed in the liquid metal pool as presented in Section III–C).

F. Formation Mechanism of Inclusions in Liquid Metal Pool and Remelted Ingot

Even though all oxide and sulfide inclusions from the electrode can be removed during the ESR for some cases, it is a fact that fresh oxide inclusions would form during cooling and solidification of liquid steel in mold (even in liquid metal pool for particular cases). These fresh oxide inclusions could hardly be removed during the ESR,[65–67] even if fresh inclusion removal by floating up is possible in liquid metal pool. Nearly all, if not all, fresh oxide inclusions would remain until in as-cast ingot.[46, 67] The work by Fu et al.,[66] Kay et al.,[65] and Mitchell[67] demonstrated that most (even
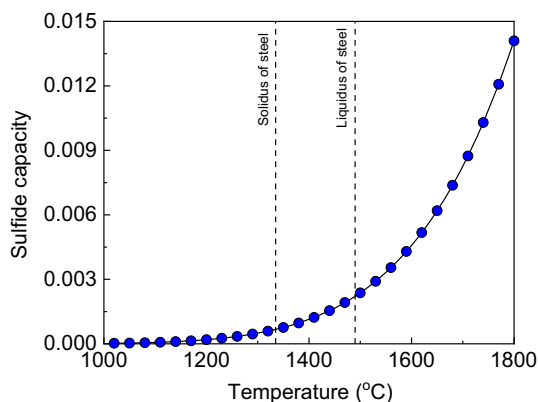
Table V. Parameters Used for Calculating ξ

Unary	ξ_i
MnO	-36626.4629
SiO$_2$	168872.587
Al$_2$O$_3$	157705.276
CaO	-33099.425

Binary interaction	ξ_{mix}
Al$_2$O$_3$-CaO	$y_{Al^{3+}} \cdot y_{Ca^{2+}} \cdot [98282.7968 + 55.07340941T]$
Al$_2$O$_3$-MnO	$y_{Al^{3+}} \cdot y_{Mn^{2+}} \cdot [433987.403 + 249.121594T \cdot (y_{Al^{3+}} - y_{Mn^{2+}})]$
Al$_2$O$_3$-SiO$_2$	$y_{Al^{3+}} \cdot y_{Si^{4+}} \cdot [186850.468]$
Ca-SiO$_2$	$y_{Ca^{2+}} \cdot y_{Si^{4+}} \cdot [97271.7695 + 72.8749746T]$
MnO-SiO$_2$	$y_{Mn^{2+}} \cdot y_{Si^{4+}} \cdot$ $[-322911.470 + 212.029980T + 134860.658 \cdot (y_{Mn^{2+}} - y_{Si^{4+}})]$

Ternary interaction	ξ_{mix}
Al$_2$O$_3$-CaO-SiO$_2$	$y_{Al^{3+}} \cdot y_{Ca^{2+}} \cdot y_{Si^{4+}} \cdot [-2035792.64 + 686.044695T]$
Al$_2$O$_3$-MnO-SiO$_2$	$y_{Al^{3+}} \cdot y_{Mn^{2+}} \cdot y_{Si^{4+}} \cdot$ $[156584.846 - 662.494162T - 532290.311 y_{Al^{3+}}]$
CaO-MnO-SiO$_2$	$y_{Ca^{2+}} \cdot y_{Mn^{2+}} \cdot y_{Si^{4+}} \cdot$ $[-1179891.59 + 621.243714T - 1191111.79 y_{Ca^{2+}}]$

Note The data in Table V are from Ref. [64].

Fig. 16—Sulfide capacity of MnO-SiO$_2$-Al$_2$O$_3$-CaO inclusions at different temperatures.

almost all) of the inclusions in ESR ingot are the inclusions generated during the cooling and solidification of liquid steel. In contrast, Shi et al.[16] reported that the oxide inclusions in ESR ingots are originated in two ways: (1) soluble aluminum modification of the oxide inclusions from electrode, and (2) reoxidation products that generated by the reactions taking place in the liquid metal pool during protective argon gas atmosphere ESR. Persson and Mitchell[68] reported that 50 pct of the inclusions (MgO·Al$_2$O$_3$) in pilot-scale ingot come directly from the electrode without a change in the ESR process. It was reported that the fresh inclusions in the remelted ingot hold different sources.[16, 65–68] Besides understanding the removal of the inclusions from the electrode, it is quite necessary to clarify the trajectories of fresh inclusions formation during the current protective argon gas atmosphere ESR.

The inclusion observations together with the thermodynamic and kinetics calculation show that all oxide inclusions from the electrode were removed during the current during protective argon gas atmosphere ESR (dissociated into their individual chemical species in liquid steel or absorbed into molten slag), as discussed in Section III–E. The soluble aluminum and calcium react with available soluble oxygen in liquid steel (dissociated from MnO-SiO$_2$-Al$_2$O$_3$-3 mass pctCaO inclusions) to form calcium aluminate and alumina inclusions. The inclusion formation during cooling and solidification of liquid steel at equilibrium state calculated with FactSage 7.2 (FToxid and FSstel databases) is shown in Figure 17. The results depicted in Figure 17 indicate that Al$_2$O$_3$ inclusions are dominant, followed by CA6 (CaO-6Al$_2$O$_3$) across a wide temperature range (from above 1873 K (1600 °C) to around solidus temperature of the steel). The starting temperatures of CA2 (CaO-2Al$_2$O$_3$) formation during cooling of liquid steel are 1985 K, 1920 K, 1919 K (1712 °C, 1647 °C, 1646 °C, in trials R1, R3, and R5, respectively). These

minor amounts of CA2 (CaO-2Al$_2$O$_3$) gradually decrease to zero as the amount of CA6 increase during the cooling of liquid steel. The thermodynamic calculation presented in Figure 17 shows that peritectic reaction of liquid steel and CA2 takes place for forming CA6, indicating that calcium aluminate inclusions in the steel ingots are CA6.

The temperature of the liquid metal pool in the ESR exhibits in a gradient distribution [typically around 1873 K (1600 °C)].[69–71] The thermodynamic calculation of inclusion formation at equilibrium state shows that Al$_2$O$_3$ and CA6 inclusions would be generated during ESR and remain until in the remelted ingots (absence of CA2). However, the observed CaO-Al$_2$O$_3$ inclusions in both the liquid metal pool and ingots contain much higher CaO contents in comparison with the calculated CA6 (7.29 mass pct). For most cases, oxide inclusions are heterogeneous in their chemistries, and composed of multiple phases.[72,73] Thus, it is expected that the observed CaO-Al$_2$O$_3$ inclusions are not solely composed of single CA2 or CA6, but a mixture of these two phases.

The thermodynamic calculation of inclusion equilibrium formation with FactSage 7.2 (as shown in Figure 17) assumes uniform solute distribution in both the solid and liquid steel. However, this is not the case in the ESR practice because the solidification of liquid steel takes place at a high local cooling rate, resulting in inadequate diffusion of solutes in solid phase.[74] The different phases of inclusion groups are not in equilibrium state, but their compositions would move toward the expected equilibrium phases over time. To this end, the Scheil–Gulliver model included in FactSage 7.2 software was employed to predict inclusion precipitation and transformation during the non-equilibrium solidification of liquid steel. Scheil–Gulliver model assumes uniform solute distribution in the liquid and no diffusion of solutes in the solid phase.[75] The calculated results are shown in Figure 18. It can be learned from Figure 18 that CA2 is not a transient phase, but exits in a wide temperature range (from higher than 1873 K (1600 °C) to fully solid).

The relative proportion (number) of oxide inclusions does not apparently change from liquid metal pool to solidified ingot, but the Al$_2$O$_3$ contents of the observed CaO-Al$_2$O$_3$ inclusions increase (see Figure 10). It is because the relative fraction of CA6 increases during cooling of liquid steel as shown in Figure 18, resulting in an increase in the Al$_2$O$_3$ content of CaO-Al$_2$O$_3$ inclusions in remelted ingots. The mass fraction of Al$_2$O$_3$ in the CaO-Al$_2$O$_3$ inclusions in the steel samples taken from liquid metal pool decreases with increasing the SiO$_2$ content of slag. It is attributed to the reaction between SiO$_2$ in slag and soluble aluminum, resulting in lower soluble aluminum content in liquid steel (providing a smaller driving force for increasing Al$_2$O$_3$ concentration in CaO-Al$_2$O$_3$ inclusions). Note that there is no
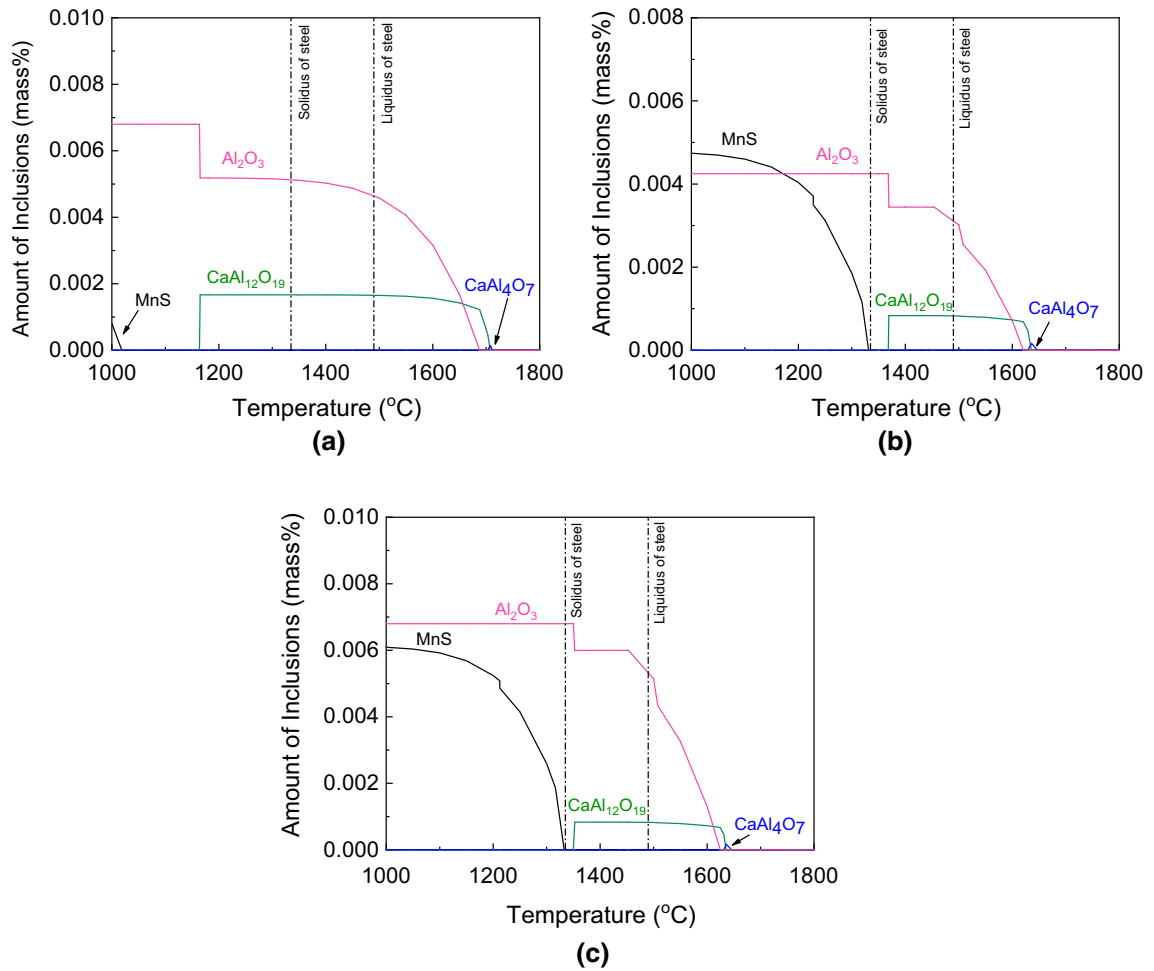
Fig. 17—Cooling curves at an equilibrium state for (*a*) D1, (*b*) D3, and (*c*) D5 calculated with FactSage 7.2.

appreciable difference in the Al_2O_3 contents of $CaO\text{-}Al_2O_3$ inclusions in the remelted ingots D1, D3, and D5 despite the slag with varying SiO_2 contents is used in the current protective argon gas atmosphere ESR.

According to the thermodynamic calculation of inclusion non-equilibrium formation using Scheil–Gulliver model, CA2 phase and CA6 phase (both of them are classified as $CaO\text{-}Al_2O_3$ inclusion) are generated during the cooling and solidification of liquid steel. The amount of CA6 is always higher than that of CA2 during the cooling and solidification of liquid steel. The $CaO\text{-}Al_2O_3$ inclusions in both liquid metal pool and ingots are mixtures of CA2 and CA6. During the cooling of liquid steel from the temperatures of 1707 °C, 1636 °C, 1630 °C in R1, R3, and R5 trials, respectively, the amount of CA2 is constant, whereas the amount of CA6 increases (see Figure 18). Therefore, the mass fraction of CA2 in $CaO\text{-}Al_2O_3$ inclusions in liquid metal pool is higher than that in the remelted ingots. The content of Al_2O_3 in $CaO\text{-}Al_2O_3$ inclusions in the ESR ingots is close to that in the calculated CA6 (92.71 mass pct Al_2O_3). This thermodynamic analysis is supported by the experimental observations that the Al_2O_3 contents of

$CaO\text{-}Al_2O_3$ inclusions in the ingots D1, D3, and D5 are 91.47 mass pct, 90.86 mass pct, and 90.22 mass pct, respectively.

IV. CONCLUSIONS

The loss and pickup of alloying elements in a heat-resistant steel during protective argon gas atmosphere ESR were investigated. The transformation and removal of $MnO\text{-}SiO_2\text{-}Al_2O_3\text{-}CaO$ inclusions and patch-type MnS inclusions during the protective argon gas atmosphere ESR were studied. The formation of Al_2O_3 and $CaO\text{-}Al_2O_3$ inclusions were ascertained. The following conclusions are obtained:

(1) The boron content of the steel increases from 0.0089 mass pct in the electrode to 0.0280 to 0.0340 mass pct after protective argon gas atmosphere ESR, which is accompanied by an increase in the aluminum content from 0.0010 mass pct in the electrode to 0.0079-0.0400 mass pct. The pickup degree of both boron and aluminum in liquid steel during protective argon gas atmosphere ESR was suppressed with increasing the SiO_2 content of slag
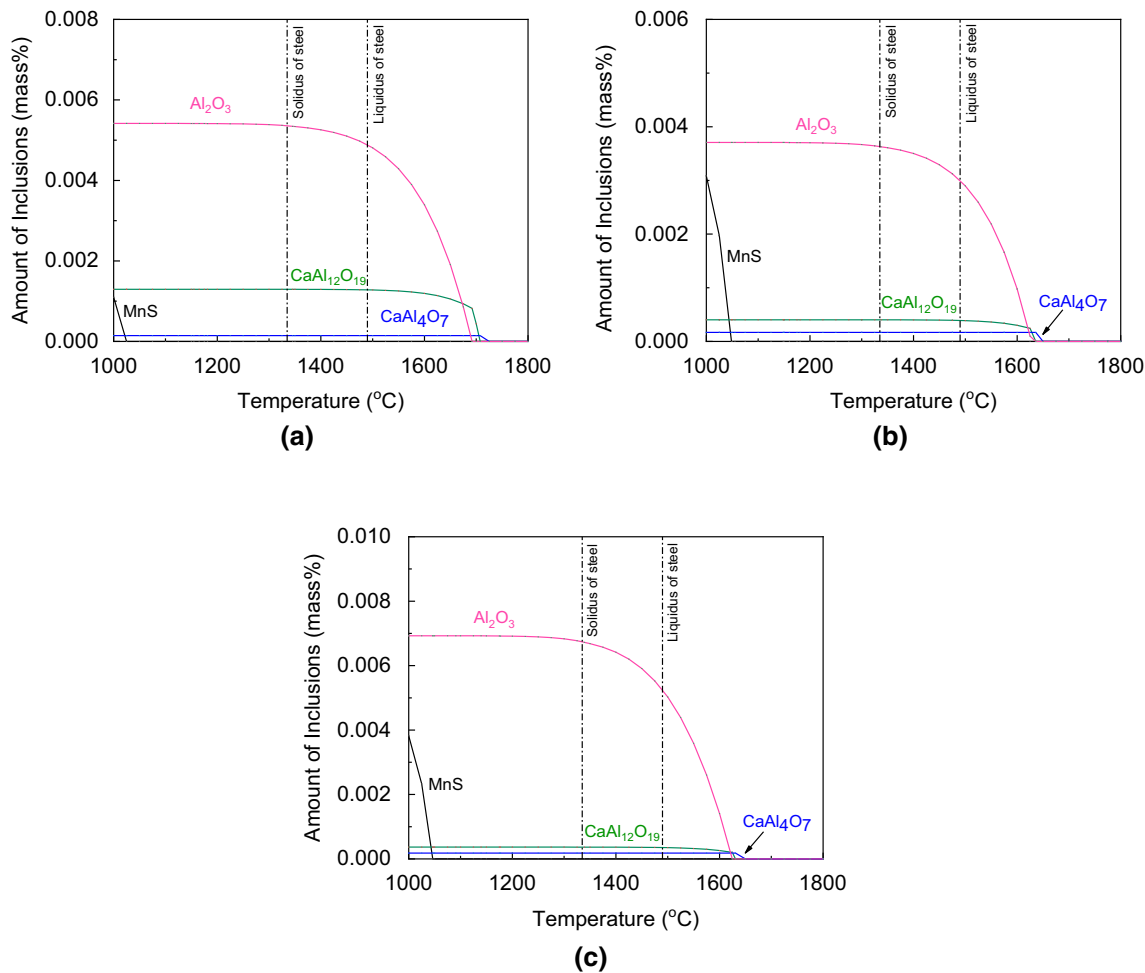
Fig. 18—Scheil–Gulliver cooling curve of (*a*) D1, (*b*) D3, and (*c*) D5 calculated with FactSage 7.2.

(from 0.92 mass pct, 5.00 mass pct to 9.00 mass pct) through inhibiting the reactions of Al_2O_3 and B_2O_3 in the slag with soluble silicon in liquid steel.

(2) The oxide inclusions in the electrode are quaternary liquid MnO-SiO_2-Al_2O_3-CaO (containing around 3 mass pct CaO) invariably along with patch-type MnS. The oxide inclusions from the electrode are fully removed before liquid metal droplets enter into liquid metal pool during the protective argon gas atmosphere ESR process in two ways: a portion of these oxide inclusions were decomposed into its individual chemical species into liquid steel, and the others were absorbed into molten slag.

(3) A part of patch-type MnS inclusions in the electrode are dissociated into soluble sulfur and manganese in liquid steel before they enter into liquid metal pool during protective argon gas atmosphere ESR, and the others are dissolved into MnO-SiO_2-Al_2O_3-CaO inclusions. MnS inclusions in MnO-SiO_2-Al_2O_3-CaO inclusion were removed together with this oxide inclusion through being decomposed into liquid steel or absorbed by molten slag.

(4) A kinetic model for describing and predicting oxide inclusion removal by slag adsorption was developed.

The oxide inclusions smaller than 3.9 *μ*m from the electrode were removed through dissociating into their specific chemical species in liquid steel. The critical size of the inclusions that would be absorbed by molten slag is 3.9 *μ*m. The inclusion with larger size is more favorable to be absorbed by molten slag. 16 pct of oxide inclusions (in number fraction) are absorbed by molten slag at the electrode tip during the protective argon gas atmosphere ESR.

(5) The inclusions in liquid metal pool and ingots are the newly formed Al_2O_3 (around 80 pct in number fraction) and CaO-Al_2O_3. The number fraction of CaO-Al_2O_3 inclusions did not apparently change from liquid metal pool to ingots, but their Al_2O_3 contents increase. The Al_2O_3 content in CaO-Al_2O_3 inclusions in the liquid metal pool significantly decreases with the increase in SiO_2 content of the slag because of the suppression of soluble aluminum pickup. The compositions of CaO-Al_2O_3 inclusions only slightly differ in the different ESR ingots even though the SiO_2 contents of the slag are significantly different for protective argon gas atmosphere ESR trials.

(6) The oxygen content of heat-resistant steel was decreased from 0.0054 mass pct in the electrode to

0.0021 mass pct to 0.0035 mass pct after protective argon gas atmosphere ESR. The size of inclusions was significantly reduced after protective argon gas atmosphere ESR, in parallel with a considerable decrease in the number density of inclusions. The generation of fresh oxide inclusions during the cooling and solidification of liquid steel leads to an increase in both the size and number density of the inclusions. The varying SiO_2 additions in slag have no influence on the size distribution and number density of inclusions in liquid metal pool and ingots.

CONFLICT OF INTEREST

On behalf of all authors, the corresponding author states that there is no conflict of interest.

REFERENCES

1. T.U Kern, K.H. Mayer, B. Donth, G. Zeiler, and A. DiGianfrancesco: in *Proc. 9th Liege COST Conf. Mater. Adv. Power Eng. 2010*, 2010, pp. 29–38.
2. F. Abe, M. Tabuchi, H. Semba, M. Yoshizawa, N. Komai, and A. Fujita: in *Proc. 5th Int. Conf. on Advances in Materials Technology for Fossil Power Plants*, 2007, pp. 92–106.
3. P. Yan, Z. Liu, H. Bao, Y. Weng, and W. Liu: *Mater. Sci. Eng. A*, 2013, vol. 588, pp. 22–28.
4. Q. Li, Z.Z. Chen, X.L. Jiang, Z.D. Liu, and L. Zuo: *Iron steel*, 2021, vol. 56, pp. 40–49. (**in Chinese**).
5. E. Plesiutschnig, C. Beal, S. Paul, G. Zeiler, S. Mitsche, and C. Sommitsch: *Mater. Sci. Forum*, 2014, vol. 783–786, pp. 1867–871.
6. V. Vicario, T. Brambilla, and M. Colnaghi: in *Proc. 19th Int. Forgemasters Meeting*, 2014, pp. 328-32.
7. G. Zeiler, R. Bauer, and A. Putschoegl: *Metall. Ital.*, 2010, vol. 6, pp. 33–40.
8. D.S. Kim, G.J. Lee, M.B. Lee, J.I. Hur, and J.W. Lee: in *Proc. 2015 Int. Symp. on Liquid Metal Processing and Casting*, 2015, pp. 43–52.
9. M. Knabl, K. Eynatten, M. Kubin, A. Scheriau, and H. Holzgruber: *BHM Berg-und Hüttenmännische Monatshefte*, 2018, vol. 163, pp. 355–60.
10. A. Benaarbia, X. Xu, W. Sun, A.A. Becker, and S. Osgerby: *Int. J. Fatigue*, 2020, vol. 131, 105270.
11. D.S. Kim, S.K. Jo, K.R. Lee, S.T. Kang, and J.T. Kim: *AISTech 2006 Proceedings*, 2006, pp. 561–71.
12. A.D. Gianfrancesco, L. Cipolla, M. Paura, S. Tiberi Vipraio, D. Venditti, S.Neri, and M. Calderini: in *International Conference on Advances in Materials Technology for Fossil Power Plants*, 2010, pp. 342–60.
13. L. Li, R. MacLachlan, M.A.E. Jepson, and R. Thomson: *Metall. Mater. Trans. A*, 2013, vol. 44, pp. 3411–18.
14. F. Abe: *Mater. Sci. Eng. A*, 2009, vol. 510–511, pp. 64–69.
15. J. Ba, J. Gao, S. Bo, and Q. Yang: *Heavy Casting and Forging*, 2018, (3), pp. 1–7.
16. C.B. Shi, H. Wang, and J. Li: *Metall. Mater. Trans. B*, 2018, vol. 49, pp. 1675–89.
17. C.B. Shi, J. Li, J.W. Cho, F. Jiang, and I.H. Jung: *Metall. Mater. Trans. B*, 2015, vol. 46, pp. 2110–20.
18. J. Fedko and M. Krucinski: *Ironmaking Steelmaking*, 1989, vol. 16, pp. 116–22.
19. E.Y. Kolpishon, A.N. Mal'ginov, A.N. Romashkin, V.A. Durynin, S.Y. Afanas'ev, E.V. Shitov, L.T. Afanas'eva, and Y.M. Batov: *Russian Metallurgy* (*Metally*), 2010, vol. 2010, pp. 489–93.
20. E.M. O'Hara, B. Phelan, S. Osgerby, R.A. Barrett, R. Raghavendra, S.B. Leen, and N.M. Harrison: *Materialia*, 2020, vol. 12, 100683.
21. M. Banaszkiewicz: *Int. J. Fatigue*, 2018, vol. 113, pp. 311–23.
22. E.M. O'Hara, N.M. Harrison, B.K. Polomski, R.A. Barrett, and S.B. Leen: *Fatigue Fract. Eng. Mater. Struct.*, 2018, vol. 41, pp. 2288–2304.
23. X. Xu, A. Benaarbia, D.J. Allen, M.A.E. Jepson, and W. Sun: *Mater. Sci. Eng. A*, 2020, vol. 791, 139546.
24. C.B. Shi, S.J. Wang, J. Li, and J.W. Cho: *J. Iron Steel Res. Int.*, 2021, vol. 28, pp. 1483–1503.
25. T.J. Wen, Q. Ren, L.F. Zhang, J.J. Wang, Y. Ren, J. Zhang, W. Yang, and A.J. Xu: *Steel Res. Int.*, 2021, vol. 92, p. 2000629.
26. X.Y. Gao, L. Zhang, X.H. Qu, Y.F. Luan, and X.W. Chen: *Metall. Res. Technol.*, 2020, vol. 117, pp. 501–09.
27. C.B. Shi: *ISIJ Int.*, 2020, vol. 60, pp. 1083–96.
28. A. Fujio, H. Kutsumi, H. Haruyama, and H. Okubo: *Corros. Sci.*, 2017, vol. 114, pp. 1–9.
29. A. Fujio: *Materials for Ultra-Supercritical and Advanced Ultra-Supercritical Power Plants*, in: Augusto Di Gianfrancesco (Eds.), Woodhead Publishing Limited, Cambridge 2017, pp. 323–74 (Chapter 10).
30. G.K. Sigworth and J.F. Elliott: *Met. Sci.*, 1974, vol. 8, pp. 298–310.
31. C.B. Shi, Y. Huang, J.X. Zhang, J. Li, and X. Zheng: *Int. J. Miner. Metall. Mater.*, 2021, vol. 28, pp. 18–29.
32. W. Holzgruber, K. Petersen, and P. E. Schneider: [in] *Trans. Int. Vacuum Metall. Conf.*, 1968, pp. 499–523.
33. E. Plöckinger: *J. Iron Steel Inst.*, 1973, vol. 211, pp. 533–41.
34. C.B. Shi: Behaviour and Control Technique of Oxygen and Inclusions during Protective Atmosphere Electroslag Remelting Process [Dissertation], University of Science and Technology Beijing, Beijing, 2012, pp. 5.
35. J.H. Wei and A. Mitchell: *Acta Metall. Sin.*, 1984, vol. 20, pp. 261–79.
36. A. Mitchell, J. Szekely, and J.F. Elliott: *Electroslag Refining*, The Iron and Steel Institute, London, 1973, pp. 3–15.
37. M.E. Fraser and A. Mitchell: *Ironmak. Steelmak.*, 1976, vol. 3, pp. 279–87.
38. S.J. Li, G.G. Cheng, L. Yang, L. Chen, Q.Z. Yan, and C.W. Li: *ISIJ Int.*, 2017, vol. 57, pp. 713–22.
39. S.C. Duan, M.J. Lee, D.S. Kim, and J.H. Park: *J. Mater. Res. Technol.*, 2021, vol. 17, pp. 574–85.
40. C. Wagner: *Thermodynamics of Alloys*, Addison-Wesley Press, Cambridge, 1952, p. 51.
41. H. Ohta and H. Suito: *Metall. Mater. Trans. B*, 1996, vol. 27, pp. 943–53.
42. H. Ono-Nakazato, K. Taguchi, R. Maruo, and T. Usui: *ISIJ Int.*, 2007, vol. 47, pp. 365–69.
43. The Japan Society for the Promotion of Science: *The 19th Committee on Steelmaking: Steelmaking Data Sourcebook*, Gordon and Breach Science Publishers, New York, 1988.
44. C.B. Shi, X.C. Chen, H.J. Guo, Z.J. Zhu, and H. Ren: *Steel Res. Int.*, 2012, vol. 83, pp. 472–86.
45. P.P. Evseyev and A.F. Filippov: *Izvest. Akad. Nauk SSSR Metally*, 1968, vol. 3, pp. 41–43.
46. C.B. Shi and J.H. Park: *Metall. Mater. Trans. B*, 2019, vol. 50, pp. 1139–47.
47. Y.W. Dong, Z.H. Jiang, Y.L. Cao, A. Yu, and D. Hou: *Metall. Mater. Trans. B*, 2014, vol. 45, pp. 1315–24.
48. R.G. Baligidad, U. Prakash, V.R. Rao, P.K. Rao, and N.B. Ballal: *Ironmak. Steelmak.*, 1994, vol. 21, pp. 324–31.
49. Y. Li, C.Y. Chen, Z.H. Jiang, M. Sun, H. Hu, and H.B. Li: *ISIJ Int.*, 2018, vol. 58, pp. 1232–41.
50. J. Elfsberg and T. Matsushita: *Steel Res. Int.*, 2011, vol. 82, pp. 404–14.

51. L.A. Girifalco and R.J. Good: *J. Phys. Chem.*, 1957, vol. 61, pp. 904–09.
52. C. Xuan, E.S. Persson, R. Sevastopolev, and M. Nzotta: *Metall. Mater. Trans. B*, 2019, vol. 50B, pp. 1957–73.
53. K. Nakajima: *Tetsu–to–Hagané*, 1994, vol. 80, pp. 599–604.
54. K. Nakajima: *Tetsu–to–Hagané*, 1994, vol. 80, pp. 383–88.
55. J. Strandh, K. Nakajima, R. Eriksson, and P. Jönsson: *ISIJ Int.*, 2005, vol. 45, pp. 1838–47.
56. B.G. Thomas, Q. Yuan, S. Mahmood, R. Liu, and R. Chaudhary: *Metall. Mater. Trans. B*, 2014, vol. 45B, pp. 22–35.
57. V.D. Eisenhüttenleute: *Slag Atlas*, 2nd ed. Woodhead Publishing Limited, Cambridge, 1995, p. 44.
58. Q. Wang, K.D. Squires, M. Chen, and J.B. McLaughlin: On the role of the lift force in turbulence simulations of particle deposition. *Int. J. Multiph. Flow*, 1997, vol. 23, pp. 749–63.
59. K. Takahashi and S. Taniguchi: *ISIJ Int.*, 2003, vol. 43, pp. 820–27.
60. C.B. Shi, H.J. Guo, X.C. Chen, X.L. Sun, and J. Fu: *Special Steel*, 2013, vol. 34, pp. 11–15.
61. S.J. Li, G.G. Cheng, Z.Q. Miao, L. Chen, C.W. Li, and X.Y. Jiang: *ISIJ Int.*, 2017, vol. 57, pp. 2148–56.
62. H.S. Kim, H.G. Lee, and K.S. OH: *Metall Mater. Trans. A*, 2001, vol. 32A, pp. 1519–25.
63. H. Doostmohammadi, P.G. Jönsson, J. Komenda, and S. Hagman: *Steel Res. Int.*, 2010, vol. 81, pp. 142–49.
64. M.M. Nzotta, D. Sichen, and S. Seetharaman: *ISIJ Int.*, 1998, vol. 38, pp. 1170–79.
65. D.A.R. Kay and R.J. Pomfret: *J. Iron Steel Inst.*, 1971, vol. 209, pp. 962–65.
66. J. Fu and J. Zhu: *Acta Metall. Sin.*, 1964, vol. 7, pp. 250–62.
67. A. Mitchell: *Ironmak. Steelmak.*, 1974, vol. 1, pp. 172–79.
68. E.S. Persson, A. Karasev, A. Mitchell, and P.G. Jönsson: *Metals*, 2020, vol. 10, pp. 1620–35.
69. J. Fu, C. Chen, E. Chen, and Y. Wang: *Acta Metall. Sin.*, 1979, vol. 15, pp. 44–50.
70. M. Choudhary and J. Szekely: *Metall. Trans. B*, 1980, vol. 11B, pp. 439–53.
71. Y. Dong, Z. Hou, Z. Jiang, H. Cao, Q. Feng, and Y. Cao: *Metall. Mater. Trans. B*, 2018, vol. 49B, pp. 349–60.
72. N. Choi, K.R. Lim, Y.S. Na, U. Glatzel, and J.H. Park: *J. Alloys Compd.*, 2018, vol. 763, pp. 546–57.
73. S.P.T. Piva and P.C. Pistorius: *Metall. Mater. Trans. B*, 2021, vol. 52, pp. 6–16.
74. C.B. Shi, X. Zheng, Z.B. Yang, P. Lan, J. Li, and F. Jiang: *Met. Mater. Int.*, 2021, vol. 27, pp. 3603–16.
75. Q. Chen and B. Sundman: *Mater. Trans.*, 2002, vol. 43, pp. 551–59.